Iowa State University
Digital Repository

2010

Modeling and grasping of thin deformable objects

Jiang Tian
Iowa State University

Modeling and grasping of thin deformable objects

by

Jiang Tian

A dissertation submitted to the graduate faculty

in partial fulfillment of the requirements for the degree of

DOCTOR OF PHILOSOPHY

Major: Computer Science

Program of Study Committee:
Yan-Bin Jia, Major Professor
David Fernández-Baca
Greg R. Luecke
James Oliver
Guang Song

Iowa State University

Ames, Iowa

2010

DEDICATION

I would like to dedicate this thesis to my family and to my girlfriend Wenjun Li without whose support I would not have been able to complete this work.

ACKNOWLEDGEMENTS

I am extremely lucky that I have support, encouragement, and inspiration from many people, without whom this work would not have been possible.

My greatest gratitude goes to my advisor Dr. Yan-Bin Jia for his guidance and consistent support. His knowledgeable, wise and inspiring discussions have guided me through my whole Ph.D. career. It was such a pleasure to work with him for all these years. Facing so many obstacles, I am lucky that he has always been there to show me the right direction and influenced me as an active thinker. Thank you, Professor Jia!

I am greatly thankful to other members of my committee, Dr. David Fernández-Baca, Dr. Greg R. Luecke, Dr. James Oliver, and Dr. Guang Song for their time and input. I am really fortunate to learn from these dedicated professors.

The Robotics Laboratory has been a great place to learn and do research. I would also like to thank my labmates HyunTae Na, Feng Guo, Rinat Ibrayev, Liangchuan Mi, and Theresa Driscoll for sharing their time during my Ph.D. career.

I wish to thank my friends Taiming Feng, Qingluan Xue, Ru He, Ge Xu, Xia Wang, Wei Zhang, Tsing-yi Jiang, Chuang Wang, Hua Qin, Zi Li, Fuchao Zhou, Yueran Yang and Yetian Chen for making this place so pleasant to be in.

TABLE OF CONTENTS

LIST OF TABLES

LIST OF FIGURES

ABSTRACT

Deformable modeling of thin shell-like and other objects have potential application in robot grasping, medical robotics, home robots, and so on. The ability to manipulate electrical and optical cables, rubber toys, plastic bottles, ropes, biological tissues, and organs is an important feature of robot intelligence. However, grasping of deformable objects has remained an underdeveloped research area. When a robot hand applies force to grasp a soft object, deformation will result in the enlarging of the finger contact regions and the rotation of the contact normals, which in turn will result in a changing wrench space. The varying geometry can be determined by either solving a high order differential equation or minimizing potential energy. Efficient and accurate modeling of deformations is crucial for grasp analysis. It helps us predict whether a grasp will be successful from its finger placement and exerted force, and subsequently helps us design a grasping strategy.

The first part of this thesis extends the linear and nonlinear shell theories to describe extensional, shearing, and bending strains in terms of geometric invariants including the principal curvatures and vectors, and the related directional and covariant derivatives. To our knowledge, this is the first non-parametric formulation of thin shell strains. A computational procedure for the strain energy is then offered for general parametric shells. In practice, a shell deformation is conveniently represented by a subdivision surface (12). We compare the results via potential energy minimization over a couple of benchmark problems with their analytical solutions and the results generated by two commercial softwares ABAQUS and ANSYS. Our method achieves a convergence rate an order of magnitude higher. Experimental validation involves regular and freeform shell-like objects (of various materials) grasped by a robot hand,

with the results compared against scanned 3-D data (accuracy 0.127mm). Grasped objects often undergo sizable shape changes, for which a much higher modeling accuracy can be achieved using the nonlinear elasticity theory than its linear counterpart. (In this part, the derivations of the transformation based on geometric invariants and the strain computation on a general parametric shell, and the interpretation of the geometry of strains were performed by my thesis advisor Yan-Bin Jia.)

The second part numerically studies two-finger grasping of deformable curve-like objects under frictional contacts. The action is like squeezing. Deformation is modeled by a degenerate version of the thin shell theory. Several differences from rigid body grasping are shown. First, under a squeeze, the friction cone at each finger contact rotates in a direction that depends on the deformable object's global geometry, which implies that modeling is necessary for grasp prediction. Second, the magnitude of the grasping force has to be above certain threshold to achieve equilibrium. Third, the set of feasible finger placements may increase significantly compared to that for a rigid object of the same shape. Finally, the ability to resist disturbance is bounded in the sense that increasing the magnitude of an external force may result in the breaking of the grasp.

CHAPTER 1. INTRODUCTION

Deformable objects are ubiquitous in the world surrounding us, on all aspects from daily life to industry. The need to study such shapes and model their behaviors arises in a wide range of applications. In image processing, deformable curves and surfaces have been used to segment images and volumes. The use of a deformable model usually results in a faster and more robust segmentation technique that guarantees smoothness between image slices.

In the robot-assisted surgery, since most human organs are deformable, the integration of physics-based deformable modeling has the potential to improve dexterity, precision, and speed during the surgery as well as enable some new medical methods. Virtual/augmented reality based real time and high fidelity simulation and training systems help enhancing medical capability, in which deformable modeling plays a very important role.

In haptics, touch feedback from interaction with a deformable object is directly influenced by the changing size and shape of the "contact" surface area. Both finger movement planning and force control will rely on the updates of the local shape of contact and the global shape of the object, as well as the force distribution over the contact area.

Deformation related interactive graphics applications require a continuously growing degree of visual realism. In addition to the display quality, it is especially the way in which the physical behavior eventually determines the degree of realism. All these have led to rapid development of the field, where state-of-the-art results from very different areas—theoretical physics, differential geometry, numerical methods, machine learning and computer graphics— are applied to find solutions.

1.1 Robot Grasping

In robotics, *the ability to manipulate deformable objects is an indispensable part of a robot hand's dexterity and an important feature of intelligence.* Grasping of rigid objects has been an active area in the last two decades (7). The geometric foundation for form-closure, force-closure, and equilibrium grasps is now well understood. However, grasping of deformable objects has received much less attention until recently.

For rigid objects, a grasp of an object achieves force-closure when it can resist any external wrench exerted on the grasped object. If any motion of an object is prevented, form-closure is achieved. There are numerous metrics (35; 37; 41; 78) for grasp optimization using geometric algorithms or nonlinear programming techniques.

Grasping of a deformable object is quite different from that of a rigid one. Since the number of degrees of freedom of a deformable object is infinite, it cannot be restrained by only a finite set of contacts. Consequently, form-closure is no longer applicable. Does force-closure still apply? Consider two fingers squeezing a deformable object in order to grasp it. The normal at each contact point changes its direction, so does the corresponding contact friction cone. Even if the two fingers were not initially placed at close-to-antipodal positions, the contact friction cones may have rotated toward each other, resulting in a force-closure grasp. At the same time, the magnitude of the external force is usually bounded (82). If the magnitude exceeds some limit, the grasp will be broken.

Meanwhile, grasp analysis is no longer a purely geometric problem. The wrench space will change as a result of varying geometry which can be decided by either solving high order differential equation or minimizing potential energy. Reliable modeling of the deformations is therefore crucial for grasp analysis. Most of the developed models are based on the linear elasticity, which is geometrically inexact for large deformations.

This thesis investigates shape modeling for shell-like objects that are grasped by a robot hand. A shell is a thin body bounded by two curved surfaces whose distance (i.e., the shell

thickness) is very small in comparison with the other dimensions. The thesis also includes a preliminary study of several issues in two-finger grasping of deformable thin-curve-like objects which are lower dimensional analogues to the thin shell model. The high aspect ratio of such thin objects often leads to instability in the computation. The computational cost of modeling the physical process accurately is usually high. As far as the robot grasping application is concerned, formulating models which are both physically accurate and numerically robust is very important.

1.2   Some Terminologies of Robot Grasping

- *Force-Closure*

  A grasp of an object is a force-closure grasp if arbitrary forces and moments can be exerted on this object through contacts.

- *Form-Closure*

  A grasp of an object is a form-closure grasp if any motion of the object is prevented.

- *Equilibrium*

  A grasp is in equilibrium if the sum of the forces and moments exerted on the object is zero.

- *Point contact with friction*

  A finger can exert any force inside the friction cone at the contact point.

1.3   Overview

The rest of the manuscript is organized as follows. Chapter 2 surveys related work in robot manipulation and deformable modeling. Chapter 3 goes over necessary background in differential geometry.

Chapter 4 offers a clear geometric interpretations of the shell strains. Section 4.1 presents the displacement field on a shell which describes the deformation completely. Based on the linear elasticity theory of shells, Section 4.2 establishes that the strains and strain energy of a shell under a displacement field are determined by geometric invariants of its middle surface including the two principal curvatures and two principal vectors. A computational procedure for arbitrary parametric shells is then described. Section 4.3 frames the theory of nonlinear elasticity of shells in terms of geometric invariants.

Section 4.4 sets up the subdivision-based displacement field and describes the stiffness matrix and the energy minimization process. Section 4.5 compares the simulation results over two benchmark problems with their analytical solutions and those by two commerical softwares *ABAQUS* and *ANSYS*. Section 4.6 experimentally investigates the modeling of deformable objects grasped by a BarrettHand. It compares the linear theory for small deformations and the nonlinear theory for large deformations through validation against range data generated by a 3-D scanner. We will see that nonlinear elasticity based modeling yields much more accurate results when large grasping forces are applied. Section 4.7 discusses modeling errors and future extensions.

Chapter 5 studies some issues in grasping of deformable curve-like objects. Section 5.1 transforms both linear and nonlinear modeling techniques from thin shells to thin curved objects. A cubic B-spline based nonlinear minimization of the potential energy is then described. Section 5.2 gives a frame under which two-finger squeeze grasps can be analyzed. A procedure of finding minimum graspable force magnitude is then presented. Graspable segments are compared for a rigid object and a deformable one. Effects of exerting a disturbance force to a squeeze grasp are investigated. In Chapter 6, we summarize the work and discuss the future directions.

CHAPTER 2. RELATED WORK

Grasping is a very active research area in robotics. Deformable modeling has been studied in the elasticity theory, solid mechanics, robotics, and computer graphics with a range of applications.

2.1   Robot Grasping

2.1.1   Grasping of Rigid Objects

Grasping of rigid objects has been extensively studied in the last two decades (7). Grasps can be classified into either force or form closure. They are usually investigated based on rigid body kinematics. For a rigid object, the distance between any two points on the object is frame invariant, subsequently, a set of forces applied to a rigid object at different locations can be converted to an equivalent combination of force and moment at some representative points.

A grasp of a rigid object achieves force-closure when it can resist any external wrench exerted on the grasped object (46). If any motion of an object is prevented, form-closure is achieved. In other words, form-closure means immobility, any neighboring configuration of the object will result in collision with an obstacle.

For rigid objects, grasp analysis is a purely geometric problem. Force-closure for two-finger grasping of a polygon is well understood based on geometry (54). Such a grasp is force closure if the intersection of the two contact friction cones contains the line segment connecting the two contact points. Nguyen (54) also introduced the concept of independent regions, i.e. regions on the object boundary such that a finger in each region ensures a force-

closure grasp independently of the exact contact point. He developed a geometrical approach to determine the maximum independent regions on polygonal objects using four frictionless contacts and two frictional contacts.

The problem of determining independent regions for polygonal or polyhedral objects has also been studied in (63; 64; 74; 16). Ponce et al. (65) utilized cell decomposition to compute pairs of maximal-length segments on a piecewise-smooth curved 2D object. Inside these segments, fingers can be positioned independently with force closure guaranteed.

In (61), an approach to determine independent regions on 3D objects based on initial examples was proposed. In this method, the selection of a good initial example for a given object remains as a critical step. The running time is polynomial in the number of contacts, which makes it possible to deal with grasps with relatively large numbers of contacts.

Blake (8) classified planar grasps into three types using the symmetry set, the anti-symmetry set, and the critical set along with the friction function. Jia (34) gave a fast algorithm to compute all grasps at pairs of antipodal points of a curved part based on differential geometry. He divided the part into concave and convex pieces at points of inflexion and used iterative methods including bisection to compute the grasps.

In (50), a $O(n^2 \log n)$-time algorithm was proposed to compute an optimal three-finger planar grasp by maximizing the radius of a disk centered at the origin and contained in the convex hull of the three unit normal vectors at the finger contacts. Assuming rounded finger tips, an optimality for force-closure grasps was introduced in (49) where efficient algorithms were developed for polygons and polyhedra.

Recently, an algorithm to compute form-closure grasps of 3D objects described by discrete points has been presented in (42). This algorithm is based on an iterative search through the points. Iterations are only needed to find some characteristic points of the object and they do not imply hard iterative search procedures with the risk of falling in local minimum. The method can deal with some uncertainty between the discrete points in the object description.

There are many methods for the planning of optimal grasps. A metric for measuring the

sensitivity of a grasp with respect to positioning errors can be found in (9). The grasp with insensitivity to positioning errors and ease of computation is considered good in terms of overall performance.

2.1.2 Grasping of Deformable Objects

Compared with an abundance of research in grasping of rigid objects in the last two decades, less attention has been paid to grasping of deformable objects. Wakamatsu et al. (82) examined whether force-closure and form-closure can be applied to grasping of deformable objects. Form-closure is not applicable because deformable objects have infinite degrees of freedom and cannot be constrained by a finite number of contacts. They proposed the concept of force-closure for deformable objects with bounded applied forces and defined bounded force-closure as grasps that can resist any external force within the bound.

The deformation-space (D-space) of an object was introduced in (24) as the C-space of all its mesh vertices, with modeling based on linear elasticity and frictionless contact. Deform closure is defined in a situation where positive work is needed to release the part from the frictionless contacts with fingers. This definition has frame invariant property. This model is energy-based and not experimentally verified.

Howard and Bekey (29) modeled 3D deformable objects using a interconnected particles and springs model, which formed a discretization of the initial object. The motions of particles were calculated using the Newtonian equations. A neural network was used to control a manipulator. They used deformation to learn the properties of the deformable objects, and thus determined the minimum force needed to lift the deformable object.

Work on robotic manipulation of deformable objects has been mostly limited to linear and meshed objects (84; 51). Most recently, a "fishbone" model based on differential geometry for belt objects was presented and experimentally verified (85). In this model, the deformed shape of a belt object was estimated by minimizing the potential energy. The nonlinear minimization

was performed based on the Ritz's method. The problem under geometric constraints was converted into a unconditional minimization problem with Lagrange multipliers. The model only works for *developable surfaces*.

Hirai et al. (31) proposed a control law for grasping of deformable objects, using both visual and tactile methods to control the motion of a deformable object. In their method, although uncertainties existed during the handling process, grasping and manipulation were performed simultaneously. This control strategy was carried out with no need of deformable modeling.

Saha and Isto (71) proposed a motion planning method for manipulation of deformable linear objects (DLO). This motion planner constructed a topologically-biased probabilistic roadmap in the DLO's configuration space. It also did not assume any specific physical model of the DLO. Motion plannings for several objects (rope, suture, strand etc.) could be realized by their method.

Holleman et al. (30) presented a path planning algorithm for a flexible surface patch. They used a Bézier surface and an approximate energy function to model deformation of the patch. This energy model penalized deformations that induce high curvatures, extension, and shear of the surface. They presented experimental results of paths planned for parts generated by a search graph using probabilistic roadmap.

Knotting of flexible linear object such as a wire or rope can be easily done with a vision system (47). A recognition method was proposed to obtain the structure of rope from sensor information through the cameras when a robot manipulates a rope. Two knot invariants, Jones and Bracket Polynomials, were utilized. Unknotting (40), and knotting (83) are the typical manipulation operations on this type of linear objects, which can be carried out with no need of deformable modeling.

Doulgeri and Peltekis (18) created a control model for manipulating a flexible part by a dual arm system with rolling contacts on a plane. To obtain an efficient model of the part dynamics, they treated part deformations as motion of a point mass that was at the point of

maximum deformation at each contact. A feedback control strategy initially for stable grasp of a rigid object was used for a flexible object. They simulated the part motion to show the performance of their control loop.

2.2 Deformable Modeling

2.2.1 Computer Graphics

Modeling of deformation has been extensively studied in computer graphics. Gibson and Mirtich (23) gave a comprehensive review. The main objective in this field is to generate visual effects efficiently rather than to be physically accurate. Discrepancies with the theory of elasticity are tolerated, and experiments with real objects need not be conducted. For instance, the widely used formulation (75) on the surface strain energy, as the integral sum of the squares of the norms of the changes in the first and second fundamental forms, does not follow the theory of elasticity.

In this field, there are generally two approaches to modeling deformable objects: geometry-based and physics-based (23). In a geometry-based approach, splines and spline surfaces such as Bézier curves, B-splines, non-uniform rational B-splines (NURBS), are often used as representations (4; 19). In (3), for free-form deformation, the normal vector of the deformed surface can be computed from the surface normal vector of the undeformed surface and a transformation matrix. In this way, deformations can be easily combined in a hierarchical structure.

Today's interactive graphics applications, such as computer games or simulators, demand a continuously growing degree of visual realism. In addition to the display quality, it is especially the way in which the physical behavior is simulated that eventually determines the degree of realism experienced by the user. Physics-based modeling (53) of deformation takes into account the mechanics of materials and dynamics to a certain degree. It combines differential geometry, newtonian dynamics, continuum mechanics, numerical methods, vector

calculus, and computer graphics. The Finite Element Method (FEM), the Finite Differences Method, and the Finite Volume Method are powerful continuum mechanics based methods.

Mass-spring systems simply consist of point masses connected together by a network of massless springs. Though slow on simulating material with high stiffness, they are used extensively in animation (11), facial modeling (87; 76), surgery (15), and simulations of cloth (2), and animals (81). However, unlike the FEM and the Finite Differences Methods, which are built on elasticity theory, mass-spring systems are not necessarily accurate.

The skeleton-based method (45) achieves efficiency of deformable modeling by interpolation. It computes the stresses/strains only at contact points and geometrically salient points and then interpolates over the entire surface.

Deformable model-based techniques offer a powerful approach to medical image analysis. They have been applied to images generated by computed tomography (CT), magnetic resonance (MR), and ultrasound. It is especially useful in the tasks including segmentation and matching, where the traditional image processing techniques are not sufficient. The "snake model" is widely used in medical image analysis (48). Snakes are planar deformable curves that are often used to approximate edges or contours in a sequence of images. They exhibit two principal behaviours: stretching and bending. Deformation of the snake is obtained by minimizing the total potential energy.

2.2.2 Elasticity

The FEM (21; 72; 5; 22), for modeling deformations of a wide range of shapes, represents a body as a mesh structure, and computes the stress, strain, and displacement everywhere inside the body. FEMs are used to model the deformations of a wide range of shapes: fabric (13), a deformable object interacting with a human hand (26), human tissue in a surgery (10), etc.

If an elastic object is sampled over a regular spatial grid, the differential equation governing the motion can be discretized using finite differences. As far as implementation is concerned,

this method is easier than the general FEM. Pioneering usage in computer graphics was traced back in (75). The directional derivative of the energy functional was discretized using the Finite Differences Method.

The boundary element method (BEM) (33) solves displacements and forces on the boundary surface, and thus is more efficient than the FEM. Roughly speaking, the integral form of the equation of motion is transformed into a surface integral by applying the Green-Gauss theorem. The method achieves substantial speedup because the three dimensional problem is reduced to two dimensions. However, the approach only works for objects whose interior is composed of a homogeneous material.

Small deformation of a linear object can be modeled using beam elements in FEM (80). Large deformation can be modeled by the nonlinear FEM. The Cosserat formulation was introduced to describe linear object deformation (58). A Cosserat element has six degrees of freedom: three for translation and three for rotation. It can deal with geometric non-linearity. This model reduces to a system of spatial ordinary differential equations which can be solved efficiently.

Most recently, modeling based on differential geometry has been proposed by Wakamatsu and Hirai (84). Their method described linear object deformation, i.e., flexure, torsion, and extension, by four functions: three Eulerian angles and one extensional strain. The deformed shape was decided by an algorithm based on the Ritz's method. Their computation results were experimentally verified by measuring the deformed shape of a sheet of paper.

Thin shell finite elements originated in the mid-1960s. Yang et al. (88; 89) gave two comprehensive surveys on thin shell finite elements. It is well-known that the convergence of thin shell elements requires C^1 interpolation, which is difficult. From a view point of engineering, it is crucial to formulate models which are both physically accurate and numerically robust for arbitrary shapes.

The bending energy of a deformed shell contains second order derivatives of the displacement. In order to ensure that it is finite, the basis functions interpolating the displacement

field have to be square integrable. Cirak et al. (12) introduced an FEM based on subdivision surfaces which meets such requirement. Assuming linear elasticity, they presented simulation results for planar, cylindrical, and spherical shells only. The work was extended in (77) to model dynamics in textile simulation.

Other thin shell FEMs include flat plates (91), axisymmetric shells (27; 62), and curve elements (14). More recently, computational shell analysis in the FEM has employed techniques including degenerated shell approach (32), stress-resultant-based formulations (1), integration techniques (6), 3-D elasticity elements (17), etc.

Picinbono et al. (60) proposed rotation invariant nonlinear FEM to the modeling of anisotropic soft tissues for real-time simulation. They solved the problem of rotational invariance of deformations and took into account the incompressible properties of biological tissues.

For grasping, it is common to ignore dynamics in modeling deformations using energy-based methods, which allows us to treat the grasping problem quasistatically. In computer graphics field, especially for real time simulation, it is necessary to simulate *dynamic* deformable objects. In this case, the unknown position vector field is given implicitly as the solution of some differential equation. The simplest numerical integration scheme is explicit Euler integration, where the time derivatives are replaced by finite differences. Stability and accuracy are two main standards to evaluate the performance of a numerical integration method.

Geometrically nonlinear FEM has been applied to the global deformation with real-time haptics rendering for solid objects by Zhuang and Canny (90). They numerically integrated the differential equations by explicit Newmark scheme. In order to realize real-time rendering, they approximated the stiffness matrix by a diagonal matrix. This matrix was obtained by lumping the rows of the original matrix. The diagonalization process was equivalent to approximating the mass continuum as concentrated masses at each nodal point of the mesh. In this way, the distributed mass is converted to a particle system.

Linear differential equations yield linear algebraic systems which can be solved more efficiently and more stably than nonlinear ones. Unfortunately, linearized elastic forces are only

valid for small deformations. Large rotational deformations yield highly inaccurate artifacts. To remove these artifacts, Müller and Gross (52) extracted the rotation part of the deformation for each finite element and computed the forces with respect to the non-rotated reference frame. This method yields fast and stable visual results.

CHAPTER 3. SOME BACKGROUND IN DIFFERENTIAL GEOMETRY

This chapter reviews some basics in differential geometry which are needed in the following chapters. For more on elementary differential geometry, we refer to (57; 66). The reader may skip this chapter if he/she is familiar with the content.

Throughout this thesis, we will denote by f_u the derivative of a function $f(u)$ with respect to u, and by f_{uu} the second derivative with respect to the same variable. All vectors will appear in the bold face. Curves, surfaces, curvatures, and torsions will be denoted by Greek letters by convention. Points, tangents, normals and other geometric vectors will be denoted by English letters, also by convention.

3.1 Plane Curves

Let $\boldsymbol{\sigma}(u)$ be a curve in two dimensions as shown in Figure 3.1. Let $\boldsymbol{t}$ be the tangent vector of $\boldsymbol{\sigma}$. We have

$$\boldsymbol{t} = \boldsymbol{\sigma}_u. \tag{3.1}$$

The velocity of $\boldsymbol{\sigma}$ at u is the tangent vector $\boldsymbol{t}$. A curve is regular if its speed $\|\boldsymbol{t}\|$ is not zero everywhere. To make physical sense, the curve is parametrized by arc length. Such parametrization leads to a unit speed curve. Computation will easily carry over to arbitrary speed curves. The normal $\boldsymbol{n}$ of the curve is the unit vector obtained by rotating $\boldsymbol{t}$ counterclockwise by $\frac{\pi}{2}$.
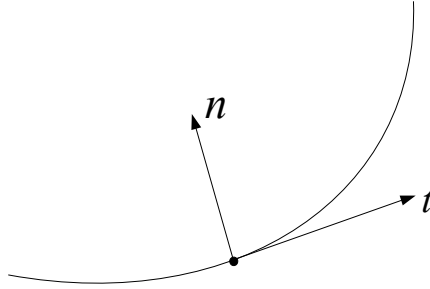
Figure 3.1 A curve.

Now let $\boldsymbol{\sigma}(u) = (x(u), y(u))^T$. Then

$$\boldsymbol{t} = \frac{(x_u, y_u)^T}{\sqrt{x_u^2 + y_u^2}},$$

$$\boldsymbol{n} = \frac{(-y_u, x_u)^T}{\sqrt{x_u^2 + y_u^2}}.$$

The curvature κ is the rate of change of direction at some point of the tangent $\boldsymbol{t}$ with respect to arc length. For a 2D curve, we have

$$\kappa = \frac{x_u y_{uu} - x_{uu} y_u}{(x_u^2 + y_u^2)^{\frac{3}{2}}}.$$

The following equations hold for vectors $\boldsymbol{t}$ and $\boldsymbol{n}$.

$$\boldsymbol{t}_u = \kappa \boldsymbol{n}, \tag{3.2}$$

$$\boldsymbol{n}_u = -\kappa \boldsymbol{t}. \tag{3.3}$$

The proof can be found from a standard differential geometry textbook.

3.2 Surfaces

Let $\boldsymbol{\sigma}(u, v)$ be a surface patch in three dimensions. It is *regular* if it is smooth and its tangent plane at every point $\boldsymbol{q}$ is spanned by the two partial derivatives $\boldsymbol{\sigma}_u$ and $\boldsymbol{\sigma}_v$. In other words, $\boldsymbol{\sigma}(u, v)$ should be smooth and $\boldsymbol{\sigma}_u \times \boldsymbol{\sigma}_v$ should be non-zero everywhere.

The unit normal to the surface is $n = \frac{\sigma_u \times \sigma_v}{\|\sigma_u \times \sigma_v\|}$. The *first fundamental form* of σ is defined as $Edu^2 + 2Fdudv + Gdv^2$, where

$$E = \sigma_u \cdot \sigma_u, \quad F = \sigma_u \cdot \sigma_v, \quad G = \sigma_v \cdot \sigma_v. \tag{3.4}$$

Denote by s the arc length of a curve on the surface patch. We have

$$ds^2 = Edu^2 + 2Fdudv + Gdv^2. \tag{3.5}$$

The *first fundamental form* relates the change in arc length to the corresponding changes in the curvilinear coordinates. The *second fundamental form* is defined as $Ldu^2 + 2Mdudv + Ndv^2$, where

$$L = \sigma_{uu} \cdot n, \quad M = \sigma_{uv} \cdot n, \quad N = \sigma_{vv} \cdot n. \tag{3.6}$$

This expression is just a convenient way of keeping track of L, M, and N.

A compact representation of the two fundamental forms comprises the following two symmetric matrices:

$$\mathcal{F}_I = \begin{pmatrix} E & F \\ F & G \end{pmatrix}, \tag{3.7}$$

$$\mathcal{F}_{II} = \begin{pmatrix} L & M \\ M & N \end{pmatrix}. \tag{3.8}$$

Denote by u an unit tangent vector at q. The normal section at q in the u direction is the intersection of the surface with a plane containing u and the surface normal n. This intersection is a curve on the surface. The corresponding curvature at q is defined as the normal curvature $\kappa_n(u)$. The maximum and minimum values of the normal curvature $\kappa_n(u)$ are the two *principal curvatures* κ_1 and κ_2 at the point q. The geometric interpretation is that they represent the maximum and minimum rates of change in geometry when passing through q at unit speed on the patch.

As far as the computation is concerned, the principal curvatures are eigenvalues of $\frac{\mathcal{F}_{II}}{\mathcal{F}_I}$. They are achieved in two orthogonal directions. These directions, denoted by unit vectors t_1

and t_2, are referred to as the *principal vectors*, where the indices are chosen so that $n = t_1 \times t_2$. The principal vectors are linear combinations of σ_u and σ_v, which span the tangent plane at q:

$$t_1 = \xi_1 \sigma_u + \eta_1 \sigma_v, \tag{3.9}$$

$$t_2 = \xi_2 \sigma_u + \eta_2 \sigma_v. \tag{3.10}$$

Here $(\xi_1, \eta_1)^T$ and $(\xi_2, \eta_2)^T$ are the eigenvectors of $\mathcal{F}_I^{-1} \mathcal{F}_{II}$ corresponding to κ_1 and κ_2, respectively. The three vectors n, t_1, and t_2 define the *Darboux frame* at the point q as shown in Figure 3.2.
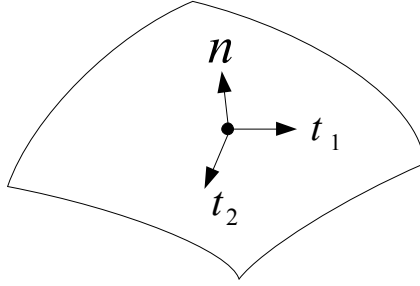
Figure 3.2   Darboux frame.

The normal curvature at q in the direction $u = cos\theta t_1 + sin\theta t_2$ is

$$\kappa_n(u) = \kappa_1 cos^2\theta + \kappa_2 sin^2\theta. \tag{3.11}$$

If the normal curvature $\kappa_n(u)$ is constant on all unit tangent vectors, the point q is called *umbilic*. In this case, geometric variation is the same in every tangent direction. Any two orthogonal directions on the tangent plane can be selected as t_1 and t_2. If q is not a umbilic point, which means $\kappa_1 \neq \kappa_2$, there are exactly two principal directions and they are orthogonal.

The *Gaussian* and *mean curvatures* are respectively the determinant and half the trace of the matrix $\frac{\mathcal{F}_{II}}{\mathcal{F}_I}$:

$$K = \kappa_1 \cdot \kappa_2 = \frac{LN - M^2}{EG - F^2}, \tag{3.12}$$

$$H = \frac{\kappa_1 + \kappa_2}{2} = \frac{1}{2} \cdot \frac{EN - 2FM + GL}{EG - F^2}. \tag{3.13}$$

The *Gaussian curvature* keeps unchanged when a surface is reparametrized. In comparison, the *mean curvature* either stays the same or changes sign in this situation. A surface is flat if its *Gaussian curvature* is zero, and minimal if its *mean curvature* is zero.

A curve on the patch is called a *line of curvature* if its tangent is in a principal direction everywhere. The patch is *orthogonal* if $F = 0$ everywhere. It is *principal* if $F = M = 0$ everywhere. In other words, a principal patch is parametrized along the two lines of curvature, one in each principal direction. On such a patch, the principal curvatures are simply $\kappa_1 = \frac{L}{E}$ and $\kappa_2 = \frac{N}{G}$, respectively, and the corresponding principal vectors are $\boldsymbol{t}_1 = \frac{\boldsymbol{\sigma}_u}{\sqrt{E}}$ and $\boldsymbol{t}_2 = \frac{\boldsymbol{\sigma}_v}{\sqrt{G}}$.

On a principal patch, defining

$$A^2 = \boldsymbol{\sigma}_u \cdot \boldsymbol{\sigma}_u$$

and

$$B^2 = \boldsymbol{\sigma}_v \cdot \boldsymbol{\sigma}_v,$$

then we have

$$ds^2 = Adu^2 + Bdv^2.$$

The quantities A and B are called *Lamé coefficients or measure numbers*.

3.3 Differentiating Surface Invariants

Next, we derive derivatives of the principal curvatures and principal vectors.

3.3.1 Differentiation of Principal Curvatures

The principal curvatures can be expressed in terms of the Gaussian and mean curvatures (choosing $\kappa_1 \geq \kappa_2$) as

$$\begin{aligned}
\kappa_1 &= H + \sqrt{H^2 - K}, & (3.14)\\
\kappa_2 &= H - \sqrt{H^2 - K}. & (3.15)
\end{aligned}$$

To obtain the partial derivatives of κ_1 and κ_2 with respect to u and v from the above equations, we first differentiate the fundamental form coefficients E, F, G, L, M, N defined in (3.4) and (3.6).

$$
\begin{aligned}
E_u &= 2\boldsymbol{\sigma}_{uu} \cdot \boldsymbol{\sigma}_u, \\
E_v &= 2\boldsymbol{\sigma}_{uv} \cdot \boldsymbol{\sigma}_u, \\
F_u &= \boldsymbol{\sigma}_{uu} \cdot \boldsymbol{\sigma}_v + \boldsymbol{\sigma}_u \cdot \boldsymbol{\sigma}_{uv}, \\
F_v &= \boldsymbol{\sigma}_{uv} \cdot \boldsymbol{\sigma}_v + \boldsymbol{\sigma}_u \cdot \boldsymbol{\sigma}_{vv}, \\
G_u &= 2\boldsymbol{\sigma}_{uv} \cdot \boldsymbol{\sigma}_v, \\
G_v &= 2\boldsymbol{\sigma}_{vv} \cdot \boldsymbol{\sigma}_v.
\end{aligned}
$$

The partial derivatives of the unit normal $\boldsymbol{n}$ can be obtained as follows (66, p. 139).

$$
\begin{aligned}
\boldsymbol{n}_u &= a\boldsymbol{\sigma}_u + b\boldsymbol{\sigma}_v, \\
\boldsymbol{n}_v &= c\boldsymbol{\sigma}_u + d\boldsymbol{\sigma}_v.
\end{aligned}
$$

where

$$
\begin{pmatrix} a & c \\ b & d \end{pmatrix} = -\mathcal{F}_I^{-1}\mathcal{F}_{II} = -\frac{1}{EG - F^2} \begin{pmatrix} GL - FM & GM - FN \\ EM - FL & EN - FM \end{pmatrix}.
$$

Then we have:

$$
\begin{aligned}
L_u &= \boldsymbol{\sigma}_{uuu} \cdot \boldsymbol{n} + \boldsymbol{\sigma}_{uu} \cdot \boldsymbol{n}_u, \\
L_v &= \boldsymbol{\sigma}_{uuv} \cdot \boldsymbol{n} + \boldsymbol{\sigma}_{uu} \cdot \boldsymbol{n}_v, \\
M_u &= \boldsymbol{\sigma}_{uuv} \cdot \boldsymbol{n} + \boldsymbol{\sigma}_{uv} \cdot \boldsymbol{n}_u, \\
M_v &= \boldsymbol{\sigma}_{uvv} \cdot \boldsymbol{n} + \boldsymbol{\sigma}_{uv} \cdot \boldsymbol{n}_v, \\
N_u &= \boldsymbol{\sigma}_{uvv} \cdot \boldsymbol{n} + \boldsymbol{\sigma}_{vv} \cdot \boldsymbol{n}_u, \\
N_v &= \boldsymbol{\sigma}_{vvv} \cdot \boldsymbol{n} + \boldsymbol{\sigma}_{vv} \cdot \boldsymbol{n}_v.
\end{aligned}
$$

Finally, the partial derivatives of K and H are then computed according to (3.12) and (3.13).

3.3.2 Coefficients of Principal Vectors

Next, we derive the four coefficients $\xi_1, \eta_1, \xi_2, \eta_2$ in (3.9) and (3.10) as well as their partial derivatives with respect to u and v. Since the principal curvatures κ_i, $i = 1, 2$, are eigenvalues of the matrix $\mathcal{F}_I^{-1} \mathcal{F}_{II}$, we have

$$
\begin{aligned}
0 &= \det(\mathcal{F}_{II} - \kappa_i \mathcal{F}_I) \\
&= (L - \kappa_i E) \cdot (N - \kappa_i G) - (M - \kappa_i F)^2.
\end{aligned}
\tag{3.16}
$$

There are two cases: (a) $L - \kappa_i E = N - \kappa_i G = 0$ for $i = 1$ or 2, and (b) either $L - \kappa_i E \neq 0$ or $N - \kappa_i G \neq 0$ for both $i = 1$ and $i = 2$.

In case (a), $M - \kappa_i F = 0$ by (3.16). So $\mathcal{F}_{II} - \kappa_i \mathcal{F}_I = 0$, i.e.,

$$
\mathcal{F}_I^{-1} \mathcal{F}_{II} = \kappa_i I_2,
$$

where I_2 is the 2×2 identity matrix. The two eigenvalues of $\mathcal{F}^{-1} \mathcal{F}_{II}$, namely, κ_1 and κ_2, must be equal. Any tangent vector is a principal vector. We let

$$
\boldsymbol{t}_1 = \frac{\boldsymbol{\sigma}_u}{\sqrt{E}}, \quad \text{with} \quad \begin{pmatrix} \xi_1 \\ \eta_1 \end{pmatrix} = \begin{pmatrix} \frac{1}{\sqrt{E}} \\ 0 \end{pmatrix} \quad \text{by (3.9)}.
$$

The other principal vector $\boldsymbol{t}_2 = \xi_2 \boldsymbol{\sigma}_v + \eta_2 \boldsymbol{\sigma}_v$ is orthogonal to $\boldsymbol{t}_1$. So

$$
(\xi_2 \boldsymbol{\sigma}_u + \eta_2 \boldsymbol{\sigma}_v) \cdot \boldsymbol{\sigma}_u = 0, \quad \text{i.e.,} \quad \xi_2 E + \eta_2 F = 0.
\tag{3.17}
$$

To determine ξ_2 and η_2, we need to use one more constraint: $\boldsymbol{t}_2 \cdot \boldsymbol{t}_2 = 1$, which is rewritten as follows,

$$
E\xi_2^2 + 2F\xi_2\eta_2 + G\eta_2^2 = 1.
\tag{3.18}
$$

Substituting (3.17) into (3.18) yields

$$
\xi_2 = \mp \sqrt{\frac{F^2}{E(EG - F^2)}}, \quad \text{and} \quad \eta_2 = \pm \sqrt{\frac{E}{EG - F^2}}.
\tag{3.19}
$$

In case (b), $L - \kappa_i E \neq 0$ or $N - \kappa_i G \neq 0$ for both $i = 1, 2$. For $i = 1, 2$, we know that

$$
(\mathcal{F}_{II} - \kappa_i \mathcal{F}_I) \begin{pmatrix} \xi_i \\ \eta_i \end{pmatrix} = 0.
\tag{3.20}
$$

Equation (3.20) expands into four scalar equations according to (3.7) and (3.8) :

$$(L - \kappa_i E)\xi_i + (M - \kappa_i F)\eta_i = 0, \tag{3.21}$$

$$(M - \kappa_i F)\xi_i + (N - \kappa_i G)\eta_i = 0. \tag{3.22}$$

Three subcases arise for each i value.

(b1) $L - \kappa_i E = 0$ but $N - \kappa_i G \neq 0$. It follows from equation (3.16) that $M - \kappa_i F = 0$. Thus equation (3.22) gives us $\eta_i = 0$. ξ_i has an exponent 2, i.e., $\boldsymbol{t}_i \cdot \boldsymbol{t}_i = E\xi_i^2 = 1$, we obtain $\xi_i = \pm\frac{1}{\sqrt{E}}$.

(b2) $L - \kappa_i E \neq 0$ but $N - \kappa_i G = 0$. This is the symmetric case of (b1). The coefficients are

$$\begin{pmatrix} \xi_i \\ \eta_i \end{pmatrix} = \begin{pmatrix} 0 \\ \pm\frac{1}{\sqrt{G}} \end{pmatrix}.$$

(b3) $L - \kappa_i E \neq 0$ and $N - \kappa_i G \neq 0$. From equation (3.21) we have

$$\xi_i = -\frac{M - \kappa_i F}{L - \kappa_i E}\eta_i. \tag{3.23}$$

Substitution of the above into (3.18) yields a quadratic equation with the solution

$$\eta_i = \pm\sqrt{\frac{L - \kappa_i E}{EN - 2FM + LG - 2\kappa_i(EG - F^2)}}. \tag{3.24}$$

In all expressions of ξ_i and η_i, the signs are chosen such that $\boldsymbol{t}_1 \times \boldsymbol{t}_2 = \boldsymbol{n}$.

The gradients $\nabla\xi_i = (\frac{\partial\xi_i}{\partial u}, \frac{\partial\xi_i}{\partial v})$ and $\nabla\eta_i = (\frac{\partial\eta_i}{\partial u}, \frac{\partial\eta_i}{\partial v})$, $i = 1, 2$, are obtained by differentiating appropriate forms of ξ_i and η_i that hold for all points in some neighborhood (not necessarily the ones at the point).

3.3.3 Directional Derivatives over Principal Vectors

Let α be a scalar function defined over a surface $\boldsymbol{\sigma}(u, v)$. Its partial derivative with respect to the parameter u can be written as follows:

$$\alpha_u = \lim_{\Delta u \to 0} \frac{\alpha(\boldsymbol{\sigma}(u + \Delta u, v)) - \alpha(\boldsymbol{\sigma}(u, v))}{\Delta u}$$

$$= \lim_{\Delta u \to 0} \frac{\alpha(\boldsymbol{\sigma}(u,v) + \boldsymbol{\sigma}_u \cdot \Delta u) - \alpha(\boldsymbol{\sigma}(u,v))}{\Delta u}$$

$$\stackrel{\text{def}}{=} \boldsymbol{\sigma}_u[\alpha], \tag{3.25}$$

where $\boldsymbol{\sigma}_u[\alpha]$ is defined as the directional derivative of α with respect to $\boldsymbol{\sigma}_u$.

Using (3.9)–(3.10), all the derivatives with respect to the principal vectors t_1, t_2 in equations, repetitive or not, can be obtained. For instance,

$$
\begin{aligned}
\boldsymbol{t}_1[\alpha] &= (\xi_1 \boldsymbol{\sigma}_u + \eta_1 \boldsymbol{\sigma}_v)[\alpha] \\
&= \xi_1 \cdot \boldsymbol{\sigma}_u[\alpha] + \eta_1 \cdot \boldsymbol{\sigma}_v[\alpha] \\
&= \xi_1 \alpha_u + \eta_1 \alpha_v \qquad \text{by (3.25)}.
\end{aligned}
$$

3.3.4 Covariant Derivatives of Principal Vectors

Let $\boldsymbol{q}$ be a point on $\boldsymbol{\sigma}(u,v)$. The principal vectors at $\boldsymbol{q}$ are t_1 and t_2. We first observe that

$$
\begin{aligned}
\frac{(\boldsymbol{t}_2)_u}{\sqrt{E}} &= \lim_{\Delta u \to 0} \frac{\boldsymbol{t}_2\Big(\boldsymbol{\sigma}(u+\Delta u, v)\Big) - \boldsymbol{t}_2(\boldsymbol{\sigma}(u,v))}{\Delta u} \cdot \frac{1}{\sqrt{E}} \\
&= \lim_{\Delta u \to 0} \frac{\boldsymbol{t}_2(\boldsymbol{q} + \boldsymbol{\sigma}_u \cdot \Delta u) - \boldsymbol{t}_2(\boldsymbol{q})}{\Delta u} \cdot \frac{1}{\sqrt{E}} \\
&= \lim_{\Delta u \sqrt{E} \to 0} \frac{\boldsymbol{t}_2\Big(\boldsymbol{q} + (\boldsymbol{\sigma}_u/\sqrt{E}) \cdot \Delta u \sqrt{E}\Big) - \boldsymbol{t}_2(\boldsymbol{q})}{\Delta u \sqrt{E}} \\
&= \lim_{\Delta s \to 0} \frac{\boldsymbol{t}_2(\boldsymbol{q} + \boldsymbol{t}_1 \cdot \Delta s) - \boldsymbol{t}_2(\boldsymbol{q})}{\Delta s} \\
&\stackrel{\text{def}}{=} \nabla_{t_1} \boldsymbol{t}_2. \tag{3.26}
\end{aligned}
$$

The *covariant derivative* $\nabla_{t_1} \boldsymbol{t}_2$ measures the rate of change of the principal vector t_2 as a unit-speed surface curve passes through the point $\boldsymbol{q}$ in the t_1 direction.

Next, we have, for $i, j = 1, 2$,

$$
\begin{aligned}
\nabla_{t_i} \boldsymbol{t}_j &= \nabla_{\xi_i \sigma_u + \eta_i \sigma_v} \boldsymbol{t}_j \\
&= \xi_i \nabla_{\sigma_u} \boldsymbol{t}_j + \eta_i \nabla_{\sigma_v} \boldsymbol{t}_j \\
&= \xi_i \nabla_{\sigma_u} (\xi_j \boldsymbol{\sigma}_u + \eta_j \boldsymbol{\sigma}_v) + \eta_i \nabla_{\sigma_v} (\xi_j \boldsymbol{\sigma}_u + \eta_j \boldsymbol{\sigma}_v). \tag{3.27}
\end{aligned}
$$

The first summand in (3.27) is computed as follows:

$$\xi_i \nabla_{\sigma_u}(\xi_j \sigma_u + \eta_j \sigma_v)$$

$$= \xi_i(\sigma_u[\xi_j] \cdot \sigma_u + \xi_j \nabla_{\sigma_u}\sigma_u + \sigma_u[\eta_j] \cdot \sigma_v + \eta_j \nabla_{\sigma_u}\sigma_v)$$

$$= \xi_i \left(\frac{\partial \xi_j}{\partial u}\sigma_u + \xi_j \sigma_{uu} + \frac{\partial \eta_j}{\partial u}\sigma_v + \eta_j \sigma_{uv} \right).$$

The first step above uses a fact about covariant derivatives: $\nabla_a(f\boldsymbol{b}) = \boldsymbol{a}[f] \cdot \boldsymbol{b} + f \cdot \nabla_a \boldsymbol{b}$. The second step uses (3.25); namely, the directional derivatives of a scalar along σ_u and σ_v, respectively, are just its partial derivatives with respect to u and v. The same rule applies to the covariant derivatives of a vector with respect to σ_u and σ_v. Similarly, we express the second summand in equation (3.27) in terms of partial derivatives with respect to u and v. Merge the resulting terms from the two summands:

$$\nabla_{t_i} t_j = \left(\xi_i \frac{\partial \xi_j}{\partial u} + \eta_i \frac{\partial \xi_j}{\partial v} \right) \sigma_u + \left(\xi_i \frac{\partial \eta_j}{\partial u} + \eta_i \frac{\partial \eta_j}{\partial v} \right) \sigma_v$$
$$+ \xi_i \xi_j \sigma_{uu} + (\xi_i \eta_j + \xi_j \eta_i)\sigma_{uv} + \eta_i \eta_j \sigma_{vv}. \tag{3.28}$$

3.3.5   Partial Derivatives of Principal Vectors

Proposition 1. *The following equations hold for partial derivatives of the principal vectors $\boldsymbol{t}_1$ and $\boldsymbol{t}_2$ on a principal patch $\boldsymbol{\sigma}(u, v)$:*

$$(\boldsymbol{t}_1)_v = \frac{(\sqrt{G})_u}{\sqrt{E}}\boldsymbol{t}_2, \tag{3.29}$$

$$(\boldsymbol{t}_2)_u = \frac{(\sqrt{E})_v}{\sqrt{G}}\boldsymbol{t}_1. \tag{3.30}$$

Proof. Due to symmetry we need only prove one equation, say, (3.30). Let us express the derivative $(\boldsymbol{t}_2)_u$ in the Darboux frame defined by $\boldsymbol{t}_1$, $\boldsymbol{t}_2$, and $\boldsymbol{n}$. Differentiating the equation $\boldsymbol{t}_2 \cdot \boldsymbol{t}_2 = 1$ with respect to u immediately yields $(\boldsymbol{t}_2)_u \cdot \boldsymbol{t}_2 = 0$. Next, we differentiate $\boldsymbol{t}_2 \cdot \boldsymbol{n} = 0$ with respect to u:

$$(\boldsymbol{t}_2)_u \cdot \boldsymbol{n} + \boldsymbol{t}_2 \cdot \boldsymbol{n}_u = 0.$$

Here n_u is the derivative of n along the principal direction $t_1 = \frac{\sigma_u}{\|\sigma_u\|}$, and hence must be a multiple of t_1.[1] Therefore, the above equation implies $(t_2)_u \cdot n = 0$.

Thus, $(t_2)_u$ has no component along t_2 or n. We need only determine its projection onto t_1. First, differentiate $\sigma_u \cdot \sigma_v = 0$ with respect to u, obtaining

$$\sigma_{uu} \cdot \sigma_v = -\sigma_u \cdot \sigma_{uv}. \tag{3.31}$$

Next, we differentiate $t_2 \cdot t_1 = 0$ with respect to u:

$$
\begin{aligned}
(t_2)_u \cdot t_1 &= -t_2 \cdot (t_1)_u \\
&= -t_2 \cdot \left(\frac{\sigma_u}{\sqrt{E}} \right)_u \\
&= -t_2 \cdot \left(\frac{\sigma_{uu}}{\sqrt{E}} + \left(\frac{1}{\sqrt{E}} \right)_u \sigma_u \right) \\
&= -t_2 \cdot \frac{\sigma_{uu}}{\sqrt{E}} \\
&= -\frac{\sigma_v \cdot \sigma_{uu}}{\sqrt{EG}} \\
&= \frac{1}{\sqrt{G}} \cdot \frac{\sigma_u \cdot \sigma_{uv}}{\sqrt{E}} \qquad \text{by (3.31)} \\
&= \frac{(\sqrt{E})_v}{\sqrt{G}}, \qquad \text{since } E = \sigma_u \cdot \sigma_u.
\end{aligned}
$$

$\square$

---

[1]One can show that $n_u = -E\kappa_1 t_1$ though the details are omitted.

CHAPTER 4. MODELING DEFORMATIONS OF GENERAL PARAMETRIC SHELLS GRASPED BY A ROBOT HAND

This chapter investigates shape modeling for shell-like objects that are grasped by a robot hand. A shell is a thin body bounded by two curved surfaces whose distance (i.e., the shell thickness) is very small in comparison with the other dimensions. The locus of points at equal distances from the two bounding surfaces is the *middle surface* of the shell.

Shells have been studied based on the geometry of their middle surfaces which are assumed to be parametrized along the lines of curvature (80; 25; 70). The expressions of extensional and shear strains, and strain energy, though derived in a local frame at every point, are still dependent on the specific parametrization rather than on geometric properties only. Such parametrizations, while always existing locally, are very difficult, if not impossible, to derive for most surfaces. Generalization of the theory to an arbitrary parametric shell is therefore not immediate. The Green-Lagrange strain tensor of a shell is presented in general curvilinear coordinates in (28; 67). However, the geometry of deformation is hidden in the heavy use of covariant and contravariant tensors for strains.

The strain energy of a deformed shell depends on the geometry of its middle surface and its thickness, all prior to the deformation, as well as the displacement field. In this chapter, we will rewrite strains in terms of geometric invariants including principal curvatures, principal vectors, and the related directional and covariant derivatives.

All shell-like objects addressed in this chapter satisfy the following three assumptions:

1. They are physically linear but geometrically either linear or nonlinear. *Physical linearity*

refers to that the elongations do not exceed the limit of proportionality so the stress-strain relation is governed by Hooke's law. *Geometric nonlinearity* refers to that the angles of rotation are of a higher order than the elongations and shears. *Geometric linearity* refers to that they are of the same order.

2. They are considered *homogeneous* and *isotropic*, i.e., having the same elastic properties in all directions.

3. Their middle surfaces are arbitrarily parametric or so approximated.

4.1   Displacement Field of a Shell

As shown in Figure 4.1, denote by $\boldsymbol{\sigma}(u, v)$ the middle surface of a thin shell with thickness h before the deformation. The parametrization is regular. Every point $\boldsymbol{p}$ in the shell is along the normal direction of some point $\boldsymbol{q}$ on the middle surface; that is, $\boldsymbol{p} = \boldsymbol{q} + z\boldsymbol{n}$, where z is the signed distance from $\boldsymbol{q}$ to $\boldsymbol{p}$.

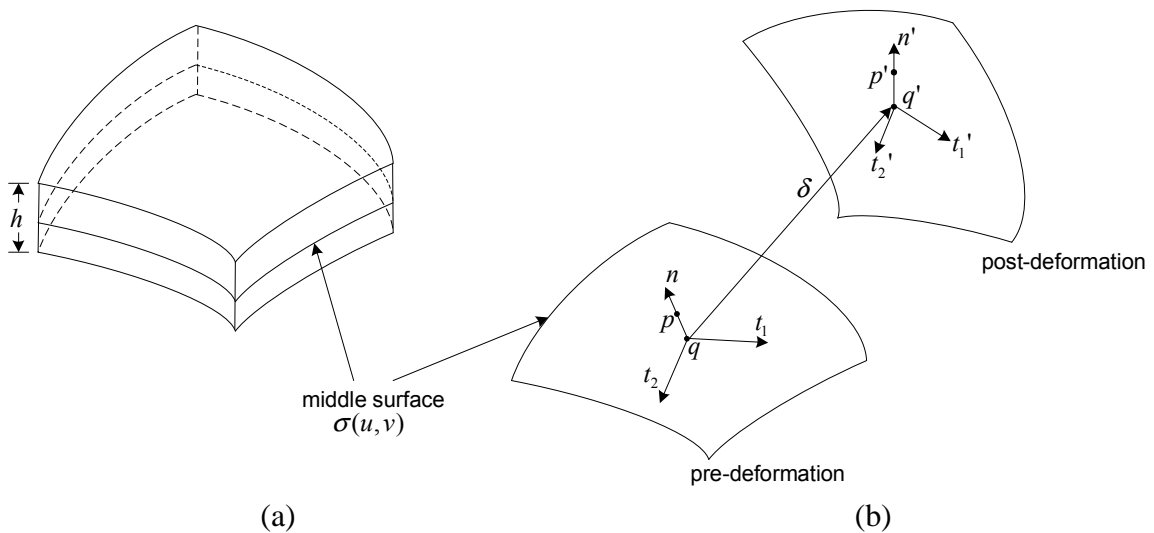(a)   (b)

Figure 4.1   Deformation of a shell. The point $\boldsymbol{p}$ in the shell is along the direction of the normal $\boldsymbol{n}$ at the point $\boldsymbol{q}$ on the middle surface. $\boldsymbol{p}'$ and $\boldsymbol{q}'$ are their displaced locations.

The displacement $\boldsymbol{\delta}(u, v)$ of $\boldsymbol{q} = \boldsymbol{\sigma}(u, v)$ can be expressed in its Darboux frame:

$$\boldsymbol{\delta}(u, v) = \alpha(u, v)\boldsymbol{t}_1 + \beta(u, v)\boldsymbol{t}_2 + \gamma(u, v)\boldsymbol{n}. \tag{4.1}$$

We call the vector field $\boldsymbol{\delta}(u, v)$ the *displacement field* of the shell. After the deformation, the new position of $\boldsymbol{q}$ is

$$\boldsymbol{q}' = \boldsymbol{\sigma}'(u, v) = \boldsymbol{\sigma}(u, v) + \boldsymbol{\delta}(u, v).$$

At the same time, from classical shell theory (56, p. 178), the displacement of $\boldsymbol{p}$ contains another term linear in the thickness z:

$$\boldsymbol{\delta}(u, v) + z \begin{pmatrix} \vartheta(u, v) \\ \varphi(u, v) \\ \chi(u, v) \end{pmatrix}. \tag{4.2}$$

The displaced position $\boldsymbol{p}'$ of the point $\boldsymbol{p}$ may not be along the normal direction of $\boldsymbol{q}'$, due to a *transverse shear strain* that acts on the surface through $\boldsymbol{p}$ and parallel to the middle surface. This type of strain tends to be much smaller than other types on a shell and is often neglected in classical shell theory (44; 80) under Kirchhoff's assumption: straight fibers normal to the middle surface of a shell before the deformation will

1. remain straight after deformation;

2. do not change their lengths;

3. and remain normal to the middle surface after deformation.

In this chapter, *we adopt Kirchhoff's assumption and do not consider transverse shear.*

The linear elasticity theory is appropriate in the situation that the deformation of a shell is small. It assumes that the magnitudes of angles of rotation do not exceed those of the elongations and shears. They are all sufficiently small when compared to unity. Under those assumptions, the squares and products of these terms are negligible. If those terms are compared with unity, they can be dropped (55). The linear theory makes no difference between the values of

the magnitudes and positions of the areas on which the stress acts for both pre-deformation and post-deformation states.

4.2 Small Deformation of a shell

Most of the literature (56; 80; 70; 25) on the linear elasticity theory of shells[1] have assumed orthogonal curvilinear coordinates along the lines of curvature. Though in theory there exists a local principal patch surrounding every point with unequal principal curvatures, most surfaces (except simple surfaces such as planes, cylinders, spheres, etc.) do not assume such a parametrization.

The exception, to our knowledge, is (28) in which general curvilinear coordinates are used in the study of plates and shells. Nevertheless, the geometric intuition behind the kinematics of deformation is made invisible amidst its heavy use of covariant and contravariant tensors to express strains and stresses. The forms of these tensors still depend on a specific parametrization rather than on just the shell geometry.

Section 4.2.1 first reviews some known results on deformations and strain energy from the linear shell theory. In Section 4.2.2, we will transform these results to make them independent of any specific parametrization, but rather dependent on geometric invariants such as principal curvatures and vectors. In the new formulation to be derived, geometric meaning of strains will be more clearly understood. Section 4.2.4 will describe how to compute strains and strain energy on an arbitrarily parametrized shell using tools from differential geometry. [2]

4.2.1 Strains in a Principal Patch

Let the shell's middle surface $\boldsymbol{\sigma}(u, v)$ be a principal patch. Under a load, at the point $\boldsymbol{q}$ on $\boldsymbol{\sigma}$ (see Figure 4.1(b)) there exist *extensional strains* ϵ_1 and ϵ_2, which are the relative

---

[1]The theory is distinguished from the membrane theory which deals with elongations but ignores shearing and bending.

[2]The mathematical derivations in Sections 4.2.2 and 4.2.3 were performed by my thesis advisor Yan-Bin Jia.

increases in lengths along the two principal directions t_1 and t_2, respectively. They are given as (25, p. 219):

$$\epsilon_1 = \frac{\alpha_u}{\sqrt{E}} + \frac{(\sqrt{E})_v}{\sqrt{EG}} \cdot \beta - \kappa_1 \gamma, \tag{4.3}$$

$$\epsilon_2 = \frac{\beta_v}{\sqrt{G}} + \frac{(\sqrt{G})_u}{\sqrt{EG}} \cdot \alpha - \kappa_2 \gamma, \tag{4.4}$$

where E, F, G are the coefficients of the middle surface's first fundamental form defined in (3.4) and κ_1 and κ_2 are the two principal curvatures, all at q.

There is also the *in-plane shear strain* ω. As shown in Figure 4.1(b), t_1' and t_2' are the unit tangents from normalizing the two partial derivatives of the displaced surface σ', respectively. These vectors are viewed as the "displaced locations" of the principal vectors t_1 and t_2. The angle between t_1' and t_2' is no longer $\pi/2$, and ω is the negative change from $\pi/2$. We have $\omega = \omega_1 + \omega_2$, where (25, p. 219)

$$\omega_1 = \frac{\alpha_v}{\sqrt{G}} - \frac{(\sqrt{G})_u}{\sqrt{EG}} \cdot \beta, \tag{4.5}$$

$$\omega_2 = \frac{\beta_u}{\sqrt{E}} - \frac{(\sqrt{E})_v}{\sqrt{EG}} \cdot \alpha. \tag{4.6}$$

The extensional and in-plane shear strains at p, which is off the shell's middle surface, will also include some components due to the rotation of the normal n. Under the assumption of small deformation, we align t_2 with t_2' and view in their common direction (see Figure 4.2). Denote by ϕ_1 the amount of rotation of the normal n' from n about the t_2 axis toward t_1. Similarly, let ϕ_2 be the amount of rotation of the normal about the t_1 axis toward t_2. We have (25, pp. 209–213)

$$\phi_1 = -\frac{\gamma_u}{\sqrt{E}} - \alpha \kappa_1, \tag{4.7}$$

$$\phi_2 = -\frac{\gamma_v}{\sqrt{G}} - \beta \kappa_2. \tag{4.8}$$
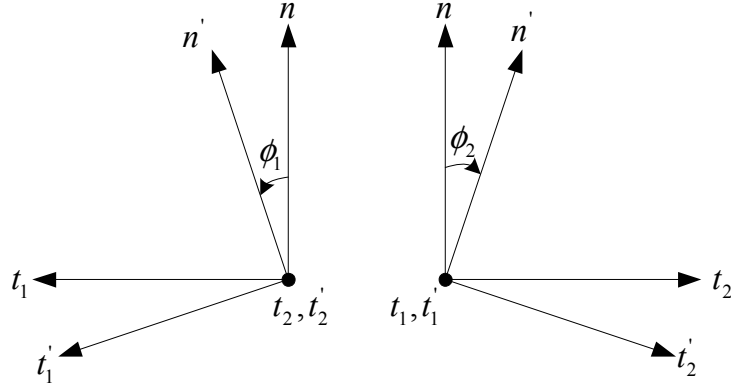
Figure 4.2   Rotation of the surface normal.

It is shown that[3] the extensional strains at $\boldsymbol{p} = \boldsymbol{q} + z\boldsymbol{n}$ are

$$\hat{\epsilon}_1 = \epsilon_1 + z\zeta_1, \tag{4.9}$$

$$\hat{\epsilon}_2 = \epsilon_2 + z\zeta_2, \tag{4.10}$$

and the shearing strain at the point is

$$\hat{\omega} = \omega + z(\tau_1 + \tau_2), \tag{4.11}$$

where the "curvature" and "torsion" terms (25, p. 219) are

$$\zeta_1 = \frac{(\phi_1)_u}{\sqrt{E}} + \frac{(\sqrt{E})_v}{\sqrt{EG}} \cdot \phi_2, \tag{4.12}$$

$$\zeta_2 = \frac{(\phi_2)_v}{\sqrt{G}} + \frac{(\sqrt{G})_u}{\sqrt{EG}} \cdot \phi_1, \tag{4.13}$$

$$\tau_1 = \frac{(\phi_1)_v}{\sqrt{G}} - \frac{(\sqrt{G})_u}{\sqrt{EG}} \cdot \phi_2 \tag{4.14}$$

$$\tau_2 = \frac{(\phi_2)_u}{\sqrt{E}} - \frac{(\sqrt{E})_v}{\sqrt{EG}} \cdot \phi_1. \tag{4.15}$$

The geometric meanings of these terms will be revealed in Section 4.2.2 after they are rewritten

into parametrization independent forms.

---

[3]by dropping all terms of order $h\kappa_1$ or $h\kappa_2$ when compared to 1.

Let e be the modulus of elasticity and μ the Poisson's constant of the shell material. We let $\tau = \tau_1 + \tau_2$. Under Hooke's law, the strain energy density is

$$dU_\epsilon = \frac{e}{2(1 - \mu^2)}(\hat{\epsilon}_1^2 + 2\mu\hat{\epsilon}_1\hat{\epsilon}_2 + \hat{\epsilon}_2^2 + \frac{1 - \mu}{2}\hat{\omega}^2)dV. \tag{4.16}$$

The strain energy can be obtained as follows.

$$\begin{aligned}
U_\epsilon &= \int_V dU_\epsilon \\
&= \frac{e}{2(1 - \mu^2)} \int_V (\hat{\epsilon}_1^2 + 2\mu\hat{\epsilon}_1\hat{\epsilon}_2 + \hat{\epsilon}_2^2 + \frac{1 - \mu}{2}\hat{\omega}^2)dV \\
&= \frac{e}{2(1 - \mu^2)} \int_\sigma \int_{-\frac{h}{2}}^{\frac{h}{2}} (\hat{\epsilon}_1^2 + 2\mu\hat{\epsilon}_1\hat{\epsilon}_2 + \hat{\epsilon}_2^2 + \frac{1 - \mu}{2}\hat{\omega}^2)dzds \\
&= \frac{e}{2(1 - \mu^2)} \int_\sigma \left\{ h\left(\epsilon_1^2 + \epsilon_2^2 + 2\mu\epsilon_1\epsilon_2 + \frac{1 - \mu}{2}\omega^2\right) \right. \\
&\quad \left. + \frac{h^3}{12}\left(\zeta_1^2 + \zeta_2^2 + 2\mu\zeta_1\zeta_2 + \frac{1 - \mu}{2}\tau^2\right)\right\} \sqrt{EG}\, dudv. \tag{4.17}
\end{aligned}$$

The linear term in h above is due to extension and shear, while the cubic term is due to bending and torsion.

4.2.2 Transformation based on Geometric Invariants

The strains (4.3)–(4.8), (4.12)–(4.15), and the strain energy formulation (4.17) are only applicable to a middle surface which is parametrized along lines of curvatures. In order to expand the application domain, these terms need to be generalized to arbitrary parametric surfaces. Rewriting the strains in terms of geometric invariants like principal curvatures and vectors that are independent of any specific parametrization is an indispensable step in the generalization. We will present this below.

The middle surface $\boldsymbol{\sigma}(u, v)$ of a shell remains to be parametrized along lines of curvatures. First, we rewrite the extensional strain (4.3) as follows:

$$\alpha_u = \boldsymbol{\sigma}_u[\alpha] \qquad\qquad \text{by (3.25).} \tag{4.18}$$

By the linearity of the directional derivative operator, we rewrite the first term in (4.3):

$$\frac{\alpha_u}{\sqrt{E}} = \frac{\boldsymbol{\sigma}_u}{\sqrt{E}}[\alpha] = \boldsymbol{t}_1[\alpha]. \tag{4.19}$$

The term $\boldsymbol{t}_1[\alpha]$ does not depend on parametrization.

As far as the second summand in (4.3) is concerned, we first have

$$\frac{(\boldsymbol{t}_2)_u}{\sqrt{E}} = \nabla_{t_1}\boldsymbol{t}_2 \qquad \text{by (3.26).} \tag{4.20}$$

Next, we make use of the following identity:

$$(\boldsymbol{t}_2)_u = \frac{(\sqrt{E})_v}{\sqrt{G}}\boldsymbol{t}_1, \tag{4.21}$$

of which the proof is given in Proposition 1 in Chapter 3. Combine equations (4.20) and (4.21):

$$\frac{(\sqrt{E})_v}{\sqrt{EG}}\boldsymbol{t}_1 = \nabla_{t_1}\boldsymbol{t}_2, \quad \text{and hence}$$

$$\frac{(\sqrt{E})_v}{\sqrt{EG}} = \nabla_{t_1}\boldsymbol{t}_2 \cdot \boldsymbol{t}_1. \tag{4.22}$$

A second identity follows by symmetry:

$$\frac{(\sqrt{G})_u}{\sqrt{EG}} = \nabla_{t_2}\boldsymbol{t}_1 \cdot \boldsymbol{t}_2. \tag{4.23}$$

Substitutions of equations (4.19) and (4.22) into (4.3) result in a formulation of the extensional strain ϵ_1 independent of the parametrization:

$$\epsilon_1 = \boldsymbol{t}_1[\alpha] + (\nabla_{t_1}\boldsymbol{t}_2 \cdot \boldsymbol{t}_1)\beta - \kappa_1\gamma$$

$$= \boldsymbol{t}_1[\alpha] + (\nabla_{t_1}\boldsymbol{t}_2 \cdot \boldsymbol{t}_1)\beta + (\nabla_{t_1}\boldsymbol{n} \cdot \boldsymbol{t}_1)\gamma. \tag{4.24}$$

The last step uses an equivalent definition of the principal curvature: $\kappa_i \stackrel{\text{def}}{=} -\nabla_{t_i}\boldsymbol{n} \cdot \boldsymbol{t}_i$.

4.2.3   Geometry of Strains

The first term $\boldsymbol{t}_1[\alpha]$ in (4.24) denotes a strain component as a result of the change rate of the displacement in the $\boldsymbol{t}_1$ direction. As shown in Figure 4.3(a), we consider a point $\boldsymbol{r}$ in the

neighborhood of q on some surface curve. This curve passes through q at unit speed in the t_1 direction. After the deformation, these two points have new positions r' and q'. Denote by q'_1 and r'_1 the corresponding projections of q' and r' onto t_1 (before the deformation). As r approaches q along the curve, the geometric interpretation of $t_1[\alpha]$ is that it measures the relative change in length between $\overline{qr}$'s projection onto t_1 and $\overline{q'_1 r'_1}$.

(a)
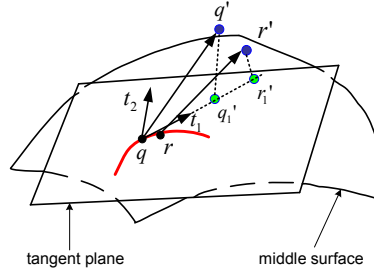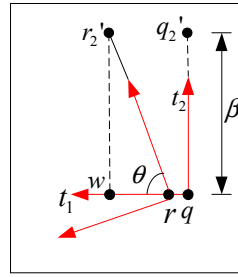
(b)

Figure 4.3   Strain along a principal direction t_1 partly due to (a) the change rate of displacement in that direction and (b) displacement in the orthogonal principal direction t_2 due to its rotation along t_1.

In order to explain the second term in (4.24), we first observe that the two principal vectors have undergone some rotations from q to r. As shown in Figure 4.3(b), since r is very close to q, it can be placed on the t_1 axis. Projecting the displaced locations q' and r' onto the corresponding second principal axes at q and r leads to two points q'_2 and r'_2. The projection of the covariant derivative $\nabla_{t_1} t_2$ onto t_1 is equal to the cosine of the angle θ normalized over $\|r - q\|$. Denote by w the projection of r'_2 onto t_1. The displacement β along t_2 also

contributes a component

$$\|\boldsymbol{w} - \boldsymbol{r}\| = \|\boldsymbol{r}_2' - \boldsymbol{r}\| \cos\theta = \beta \cos\theta$$

(normalized over $\|\boldsymbol{r} - \boldsymbol{q}\|$) to the strain ϵ_1. This component is the second term in equation (4.24).

Similarly, the third term in (4.24) is the part of the displacement γ along $\boldsymbol{n}$ involved into $\boldsymbol{t}_1$ due to the change of the normal $\boldsymbol{n}$ along $\boldsymbol{t}_1$.

By the same derivation, parametrization independent formulations can be achieved for other strain components (4.4)–(4.15):

$$\epsilon_2 = \boldsymbol{t}_2[\beta] + (\nabla_{t_2}\boldsymbol{t}_1 \cdot \boldsymbol{t}_2)\alpha + (\nabla_{t_2}\boldsymbol{n} \cdot \boldsymbol{t}_2)\gamma, \tag{4.25}$$

$$\omega_1 = \boldsymbol{t}_2[\alpha] - (\nabla_{t_2}\boldsymbol{t}_1 \cdot \boldsymbol{t}_2)\beta, \tag{4.26}$$

$$\omega_2 = \boldsymbol{t}_1[\beta] - (\nabla_{t_1}\boldsymbol{t}_2 \cdot \boldsymbol{t}_1)\alpha, \tag{4.27}$$

$$\phi_1 = -\boldsymbol{t}_1[\gamma] + (\nabla_{t_1}\boldsymbol{n} \cdot \boldsymbol{t}_1)\alpha, \tag{4.28}$$

$$\phi_2 = -\boldsymbol{t}_2[\gamma] + (\nabla_{t_2}\boldsymbol{n} \cdot \boldsymbol{t}_2)\beta, \tag{4.29}$$

$$\zeta_1 = \boldsymbol{t}_1[\phi_1] + (\nabla_{t_1}\boldsymbol{t}_2 \cdot \boldsymbol{t}_1)\phi_2, \tag{4.30}$$

$$\zeta_2 = \boldsymbol{t}_2[\phi_2] + (\nabla_{t_2}\boldsymbol{t}_1 \cdot \boldsymbol{t}_2)\phi_1, \tag{4.31}$$

$$\tau_1 = \boldsymbol{t}_2[\phi_1] - (\nabla_{t_2}\boldsymbol{t}_1 \cdot \boldsymbol{t}_2)\phi_2. \tag{4.32}$$

$$\tau_2 = \boldsymbol{t}_1[\phi_2] - (\nabla_{t_1}\boldsymbol{t}_2 \cdot \boldsymbol{t}_1)\phi_1. \tag{4.33}$$

Figure 4.4 Rotation of one principal vector toward another under deformation.

The term ϵ_2 in (4.25) has a similar geometric explanation as ϵ_1 in equation (4.24). Next, we interpret the geometric meaning of ω_1 in (4.26). As shown in Figure 4.4, every point along the principal direction $\boldsymbol{t}_2$ in a local neighborhood is displaced in the $\boldsymbol{t}_1$ direction by a value which is equal to that of the function α (see (4.1)) at that point. After the deformation, the projections of the new locations of these neighborhood points form a vector $\boldsymbol{t}_2'$ in the original tangent plane approximately. In essence, this new vector can be considered as a result of a rotation of $\boldsymbol{t}_2$ during the deformation. Since the α values of these points are usually different, $\boldsymbol{t}_2'$ is unlikely perpendicular to $\boldsymbol{t}_1$. Subsequently, the change rate $\boldsymbol{t}_2[\alpha]$ gives out the rotation of $\boldsymbol{t}_2$ toward $\boldsymbol{t}_1$ after the deformation. The second term in (4.26) represents the amount of rotation from $\boldsymbol{t}_2$ toward $\boldsymbol{t}_1$. This rotation is a result from the change in surface geometry at $\boldsymbol{q}$ along the direction $\boldsymbol{t}_2$ and the displacement β. Therefore this amount has to be subtracted from the first term, yielding exactly (4.26). By the same reasoning, ω_2 given by (4.27) is the amount of rotation from $\boldsymbol{t}_1$ toward $\boldsymbol{t}_2$. Their sum, $\omega = \omega_1 + \omega_2$, is the shearing in the tangent plane.

Similarly, the rotation from $\boldsymbol{t}_1$ toward the normal $\boldsymbol{n}$ after the deformation is the negation of ϕ_1, which is given in (4.28). Recall that no shearing happens in the normal $\boldsymbol{t}_1$-$\boldsymbol{n}$ plane under Kirchhoff's assumption. Subsequently, the rotation from $\boldsymbol{n}$ toward $\boldsymbol{t}_1$ must be ϕ_1 to ensure that the two vectors remain perpendicular to each other after the deformation. In the same way, ϕ_2 represents the rotation of $\boldsymbol{n}$ toward $\boldsymbol{t}_2$.

The geometric meanings of ζ_1, ζ_2, τ_1, and τ_2 in (4.30)–(4.33) can be explained in a similar way, though more complex. From differential geometry, we know that the derivative of a rotation of the normal $\boldsymbol{n}$ about some tangent direction is the normal curvature. The term ζ_1, referred to as *change in curvature*, accounts for the change rate of the angle ϕ_1 along the principal direction $\boldsymbol{t}_1$, plus the effect of the angle ϕ_2 due to the change of $\boldsymbol{t}_2$ along $\boldsymbol{t}_1$. The term ζ_2 can be explained similarly. Together, ζ_1 and ζ_2 measure the bending of the surfaces. The sum $\tau = \tau_1 + \tau_2$, referred to as *change in torsion*, measures the twisting of the surface due to the deformation.

In the strain energy integral (4.17), the area element $\sqrt{EG}\,dudv$ now needs to be replaced by $\sqrt{EG - F^2}\,dudv$ to be applied to a regular patch on which the two partial derivatives are not necessarily orthogonal, i.e., $F \neq 0$. Hence we have

$$U_\epsilon = \frac{e}{2(1-\mu^2)} \int_\sigma \left\{ h\left(\epsilon_1^2 + \epsilon_2^2 + 2\mu\epsilon_1\epsilon_2 + \frac{1-\mu}{2}\omega^2 \right) + \frac{h^3}{12}\left(\zeta_1^2 + \zeta_2^2 + 2\mu\zeta_1\zeta_2 + \frac{1-\mu}{2}\tau^2 \right) \right\} \sqrt{EG - F^2}\,dudv, \qquad (4.34)$$

with all strains given in (4.24)–(4.33).

4.2.4 Strain Computation for a General Parametric Shell

Since all the strain terms are expressed in terms of geometric invariants, we can compute them on an arbitrary parametric shell using tools from differential geometry. From now on, the middle surface $\boldsymbol{\sigma}(u, v)$ is *not necessarily parametrized along the lines of curvature.* To compute the strains according to equations (4.24)–(4.33), we need to be able to evaluate the directional derivatives of the principal curvatures κ_1, κ_2 with respect to the principal vectors $\boldsymbol{t}_1$ and $\boldsymbol{t}_2$, as well as the covariant derivatives $\nabla_{t_i}\boldsymbol{t}_j$, $i, j = 1, 2$ and $i \neq j$. All these derivatives have been derived in Chapter 3.

Next, we derive the derivatives of the displacements. Recall that the displacement $\boldsymbol{\delta}$ is described in the Darboux frame:

$$\boldsymbol{\delta} = \alpha\boldsymbol{t}_1 + \beta\boldsymbol{t}_2 + \gamma\boldsymbol{n},$$

where $\boldsymbol{t}_1$, $\boldsymbol{t}_2$, and $\boldsymbol{n}$ are three orthogonal unit vectors. Therefore we have:

$$\alpha = \boldsymbol{\delta} \cdot \boldsymbol{t}_1,$$
$$\beta = \boldsymbol{\delta} \cdot \boldsymbol{t}_2,$$
$$\gamma = \boldsymbol{\delta} \cdot \boldsymbol{n}.$$

All the derivatives with respect to u and v can then be obtained. For instance,

$$\alpha_u = \boldsymbol{\delta}_u \cdot \boldsymbol{t}_1 + \boldsymbol{\delta} \cdot \boldsymbol{t}_{1u},$$

$$\alpha_v = \boldsymbol{\delta}_v \cdot \boldsymbol{t}_1 + \boldsymbol{\delta} \cdot \boldsymbol{t}_{1v},$$

$$\beta_u = \boldsymbol{\delta}_u \cdot \boldsymbol{t}_2 + \boldsymbol{\delta} \cdot \boldsymbol{t}_{2u},$$

$$\beta_v = \boldsymbol{\delta}_v \cdot \boldsymbol{t}_2 + \boldsymbol{\delta} \cdot \boldsymbol{t}_{2v},$$

$$\gamma_u = \boldsymbol{\delta}_u \cdot \boldsymbol{n} + \boldsymbol{\delta} \cdot \boldsymbol{n}_u,$$

$$\gamma_v = \boldsymbol{\delta}_v \cdot \boldsymbol{n} + \boldsymbol{\delta} \cdot \boldsymbol{n}_v.$$

Similarly, the higher order derivatives can also be computed.

4.3   Large Deformation of a Shell

When a shell undergoes a large deformation, the linear elasticity theory as presented in Section 4.1 is no longer adequate. This is illustrated below using the example of a rotation about the z-axis through an angle θ:

$$\begin{pmatrix} x' \\ y' \\ z' \end{pmatrix} = \begin{pmatrix} \cos\theta & -\sin\theta & 0 \\ \sin\theta & \cos\theta & 0 \\ 0 & 0 & 1 \end{pmatrix} \begin{pmatrix} x \\ y \\ z \end{pmatrix} - \begin{pmatrix} x \\ y \\ z \end{pmatrix}.$$

No deformation happens, hence no strain along the x-axis, as confirmed by the nonlinear theory (55, p. 13):

$$\begin{aligned}
\epsilon_x &= \frac{\partial x'}{\partial x} + \frac{1}{2}\left[\left(\frac{\partial x'}{\partial x}\right)^2 + \left(\frac{\partial y'}{\partial x}\right)^2 + \left(\frac{\partial z'}{\partial x}\right)^2 \right] \\
&= \cos\theta - 1 + \frac{1}{2}\left[(\cos\theta - 1)^2 + (\sin\theta)^2 \right] \\
&= 0.
\end{aligned}$$

However, the linear elasticity theory yields a strain

$$\epsilon_x = \frac{\partial x'}{\partial x} = \cos\theta - 1, \tag{4.35}$$

which is negligible only when the rotation angle θ is small.

As before, $\boldsymbol{\sigma}(u, v)$ is the middle surface of a thin shell, in a regular parametrization. We look at a point $\boldsymbol{q} = \boldsymbol{\sigma}(u, v)$ in the middle surface with the displacement field (4.1) in the Darboux frame defined by the two principal vectors $\boldsymbol{t}_1$ and $\boldsymbol{t}_2$, and the normal $\boldsymbol{n}$ at the point. A point $\boldsymbol{p} = \boldsymbol{q} + z\boldsymbol{n}$ in the shell, which projects to $\boldsymbol{q}$, has the displacement given as (4.2).

Under Kirchhoff's assumption, at $\boldsymbol{q}$ the relative elongation ε_{33} of a fiber along the normal $\boldsymbol{n}$, and shears ε_{13} and ε_{23}, respectively, in the $\boldsymbol{t}_1$-$\boldsymbol{n}$ and $\boldsymbol{t}_2$-$\boldsymbol{n}$ planes, are zero; namely,

$$\varepsilon_{33} = \varepsilon_{13} = \varepsilon_{23} = 0. \tag{4.36}$$

Next, we present the nonlinear shell theory (55, pp. 186–193), and transform the related terms into expressions in terms of geometric invariants. First, we have the relative elongations of infinitesimal line elements starting at $\boldsymbol{q}$ as:

$$\varepsilon_{11} = \epsilon_1 + \frac{1}{2}(\epsilon_1^2 + \omega_1^2 + \phi_1^2), \tag{4.37}$$

$$\varepsilon_{22} = \epsilon_2 + \frac{1}{2}(\epsilon_2^2 + \omega_2^2 + \phi_2^2), \tag{4.38}$$

Next, the shear in the tangent plane spanned by $\boldsymbol{t}_1$ and $\boldsymbol{t}_2$ is

$$\varepsilon_{12} = \omega_1 + \omega_2 + \epsilon_1\omega_2 + \epsilon_2\omega_1 + \phi_1\phi_2. \tag{4.39}$$

In (4.37)–(4.39), ϵ_i, ω_i, ϕ_i, $i = 1, 2$, are given in (4.24)–(4.29). Note the appearance of nonlinear (quadratic) terms in equations (4.37)–(4.39). The strains ε_{ij}, $i, j = 1, 2, 3$, symmetric in the indices, together constitute the Green-Lagrange strain tensor of a shell (67, pp. 201–202).

The rate of displacement in (4.2) along the normal $\boldsymbol{n}$ at $\boldsymbol{q}$ is determined as follows:

$$\vartheta = \phi_1(1 + \epsilon_2) - \phi_2\omega_1, \tag{4.40}$$

$$\varphi = \phi_2(1 + \epsilon_1) - \phi_1\omega_2, \tag{4.41}$$

$$\chi = \epsilon_1 + \epsilon_2 + \epsilon_1\epsilon_2 - \omega_1\omega_2. \tag{4.42}$$

The relative elongations and shear at $\boldsymbol{p}$ (off the middle surface) are affected by the second order changes in geometry at its projection $\boldsymbol{q}$ in the middle surface. They are characterized

by six "curvature" terms which are rewritten in terms of t_1, t_2 and n in the same way as in Section 4.2.2:

$$\kappa_{11} = t_1[\vartheta] + (\nabla_{t_1} t_2 \cdot t_1)\varphi + (\nabla_{t_1} n \cdot t_1)\chi,$$

$$\kappa_{22} = t_2[\varphi] + (\nabla_{t_2} t_1 \cdot t_2)\vartheta + (\nabla_{t_2} n \cdot t_2)\chi,$$

$$\kappa_{12} = t_1[\varphi] - (\nabla_{t_1} t_2 \cdot t_1)\vartheta,$$

$$\kappa_{21} = t_2[\vartheta] - (\nabla_{t_2} t_1 \cdot t_2)\varphi,$$

$$\kappa_{13} = t_1[\chi] - (\nabla_{t_1} n \cdot t_1)\vartheta,$$

$$\kappa_{23} = t_2[\chi] - (\nabla_{t_2} n \cdot t_2)\varphi.$$

Among them, κ_{11} and κ_{22} describe the changes in curvature along t_1 and t_2, respectively; κ_{12} and κ_{21} together describe the twist of the middle surface in the tangent plane; and κ_{13} and κ_{23} describe the twists out of the tangent plane.

The six terms κ_{ij} form the following three parameters that together characterize the variations of the curvatures of the middle surface along the principal directions:

$$\zeta_{11} = (1 + \epsilon_1)\kappa_{11} + \omega_1\kappa_{12} - \phi_1\kappa_{13}, \tag{4.43}$$

$$\zeta_{22} = (1 + \epsilon_2)\kappa_{22} + \omega_2\kappa_{21} - \phi_2\kappa_{23}, \tag{4.44}$$

$$\zeta_{12} = (1 + \epsilon_1)\kappa_{21} + (1 + \epsilon_2)\kappa_{12}$$

$$+ \omega_2\kappa_{11} + \omega_1\kappa_{22} - \phi_2\kappa_{13} - \phi_1\kappa_{23}. \tag{4.45}$$

Finally, we have the relative tangential elongations and shear at p in terms of those at q in the middle surface:

$$\hat{\varepsilon}_{11} = \varepsilon_{11} + z\zeta_{11}, \tag{4.46}$$

$$\hat{\varepsilon}_{22} = \varepsilon_{22} + z\zeta_{22}, \tag{4.47}$$

$$\hat{\varepsilon}_{12} = \varepsilon_{12} + z\zeta_{12}. \tag{4.48}$$

Their derivation neglects terms in z^2, as well as products of z with the principal curvatures $-\nabla_{t_1} n \cdot t_1$ and $-\nabla_{t_2} n \cdot t_2$.

In the case of a small deformation, we neglect elongations and shears compared to unity, for instance, $1 + \varepsilon_1 \approx 1$ in (4.43), as well as their products (also separately with curvature terms) such as $\epsilon_1 \omega_2$ in (4.39). Equations (4.46)–(4.48) then reduce to

$$\hat{\varepsilon}_{11} = \epsilon_1 + z\kappa_{11},$$

$$\hat{\varepsilon}_{22} = \epsilon_2 + z\kappa_{22},$$

$$\hat{\varepsilon}_{12} = \omega + z(\kappa_{12} + \kappa_{21}),$$

where $\omega = \omega_1 + \omega_2$. These equations are essentially the same as (4.9)–(4.11) in the linear elasticity theory of shells, with κ_{ii} corresponding to ζ_i, κ_{12} to τ_1, and κ_{21} to τ_2.

The strain energy of the shell has a similar form as (4.34) in the linear case:

$$U_\epsilon = \frac{e}{2(1-\mu^2)} \int_\sigma \left\{ h\left(\varepsilon_{11}^2 + \varepsilon_{22}^2 + 2\mu\varepsilon_{11}\varepsilon_{22} + \frac{1-\mu}{2}\varepsilon_{12}^2 \right) \right.$$
$$\left. + \frac{h^3}{12}\left(\zeta_{11}^2 + \zeta_{22}^2 + 2\mu\zeta_{11}\zeta_{22} + \frac{1-\mu}{2}\zeta_{12}^2 \right) \right\} \sqrt{EG - F^2}\, du\, dv. \quad (4.49)$$

4.4 Energy Minimization over a Subdivision-based Displacement Field

The displacement field $\boldsymbol{\delta}(u,v) = (\alpha, \beta, \gamma)^T$ of the middle surface of a shell describes its deformation completely. At the equilibrium state, the shell has minimum total potential energy (20, p. 260), which equals its strain energy (4.34) or (4.49) minus the potential of applied loads. Applying calculus of variations, $\boldsymbol{\delta}(u,v)$ must satisfy Euler's (differential) equations. A variational method (86) usually approximates $\boldsymbol{\delta}(u,v)$ as a linear combination of some basis functions whose coefficients are determined via potential energy minimization.

Since the curvature terms ζ_1, ζ_2, and τ, or ζ_{11}, ζ_{22}, and ζ_{12} contain second order derivatives of the displacement, to ensure finite bending energy, the basis functions interpolating $\boldsymbol{\delta}(u,v)$ have to be square integrable, and their first and second-order derivatives should also be square integrable. Loop's subdivision scheme meets this requirement (43). Recently, the shape functions of subdivision surfaces have been used as finite element basis functions in simulation of thin shell deformations (12).
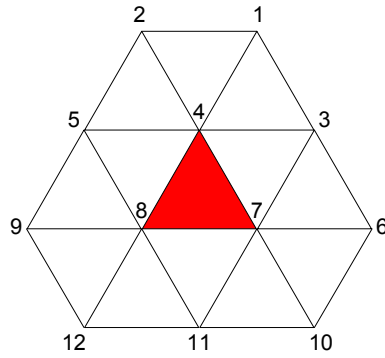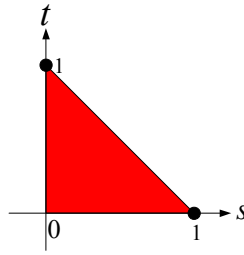
Figure 4.5 (a) A regular patch with 12 control points defining a surface element which is described in (b) barycentric coordinates s and t.

A subdivision surface, piecewise polynomial, is controlled by a triangular mesh with m vertices positioned at $\boldsymbol{x}_1, \ldots, \boldsymbol{x}_m$ in the 3-D space. Every surface element corresponds to a triangle on the mesh, and is determined by the locations of not only its three vertices but also the nine vertices in the immediate neighborhood. In Figure 4.5(a), the twelve vertices affecting the shaded element are numbered with locations $\boldsymbol{x}_i$s, respectively. A point in the element is $\sum_{i=1}^{12} b_i(s,t)\boldsymbol{x}_i$, where s and t are barycentric coordinates ranging over a unit triangle (see Figure 4.5(b)): $\{(s,t)|s \in [0,1], t \in [0, 1-s]\}$, and $b_i(s,t)$ are quartic polynomials called the *box spline basis functions* (73). Their forms are listed as:

$$b_1 = \frac{1}{12}(s^4 + 2s^3 t),$$

$$b_2 = \frac{1}{12}(s^4 + 2s^3 w),$$

$$b_3 = \frac{1}{12}(s^4 + 2s^3 w + 6s^3 t + 6s^2 tw + 12s^2 t^2 + 6st^2 w + 6st^3 + 2t^3 w + t^4),$$

$$b_4 = \frac{1}{12}(6s^4 + 24s^3 w + 24s^2 w^2 + 8sw^3 + w^4 + 24s^3 t + 60s^2 tw + 36stw^2$$

$$+ 6tw^3 + 24s^2t^2 + 36st^2w + 12t^2w^2 + 8st^3 + 6t^3w + t^4),$$

$$b_5 = \frac{1}{12}(s^4 + 6s^3w + 12s^2w^2 + 6sw^3 + w^4 + 2s^3t + 6s^2tw + 6stw^2 + 2tw^3),$$

$$b_6 = \frac{1}{12}(2st^3 + t^4),$$

$$b_7 = \frac{1}{12}(s^4 + 6s^3w + 12s^2w^2 + 6sw^3 + w^4 + 8s^3t + 36s^2tw + 36stw^2$$
$$+ 8tw^3 + 24s^2t^2 + 60st^2w + 24t^2w^2 + 24st^3 + 24t^3w + 6t^4),$$

$$b_8 = \frac{1}{12}(s^4 + 8s^3w + 24s^2w^2 + 24sw^3 + 6w^4 + 6s^3t + 36s^2tw + 60stw^2$$
$$+ 24tw^3 + 12s^2t^2 + 36st^2w + 24t^2w^2 + 6st^3 + 8t^3w + t^4),$$

$$b_9 = \frac{1}{12}(2sw^3 + w^4),$$

$$b_{10} = \frac{1}{12}(2t^3w + t^4),$$

$$b_{11} = \frac{1}{12}(2sw^3 + w^4 + 6stw^2 + 6tw^3 + 6st^2w + 12t^2w^2 + 2st^3 + 6t^3w + t^4),$$

$$b_{12} = \frac{1}{12}(w^4 + 2tw^3),$$

where $w = 1 - s - t$.

The advantage of a subdivision surface is that it can easily represent an object of arbitrary topology. The shape of a shell after a deformation usually bears topological similarity to that before the deformation. This suggests us to approximate the deformed middle surface as a subdivision surface $\boldsymbol{\sigma}'(u, v)$ over a triangular mesh that discretizes the original surface $\boldsymbol{\sigma}(u, v)$.[4] The vertices $\boldsymbol{x}_i$ of $\boldsymbol{\sigma}'(u, v)$ are at the positions $\boldsymbol{x}_i^{(0)} = \boldsymbol{\sigma}(u_i, v_i)$ before the deformation; they are later displaced by $\boldsymbol{\delta}_i = \boldsymbol{x}_i - \boldsymbol{x}_i^{(0)}$, respectively.

Every surface element S of $\boldsymbol{\sigma}'$ is parametrized with the two barycentric coordinates s and t. To compute the strain energy U_ϵ in (4.34) or (4.49), we need to set up the correspondence between (s, t) and the original parameters (u, v). The triangular mesh of $\boldsymbol{\sigma}'$ induces a subdivision of the domain of the original surface whose vertices (u_i, v_i) are the parameter values of the vertices of $\boldsymbol{x}_i$ of $\boldsymbol{\sigma}'$. In this domain subdivision, let $\boldsymbol{\sigma}'(u_k, v_k)$ be the 12 neighboring

---

[4]Subdividing the surface domain to approximate the displacement field directly does not generate a good result, as we have found out via simulation with several surfaces, because the topology of the displacement field is unknown beforehand.

vertices of $\boldsymbol{\sigma}'(u, v)$. Then

$$(u, v) = \sum_{k=1}^{12} b_k(s, t)(u_k, v_k). \tag{4.50}$$

The corresponding point on the original surface is

$$
\begin{aligned}
\boldsymbol{\sigma}(u, v) &= \boldsymbol{\sigma}\left(\sum_{i=1}^{12} b_i(s, t)(u_i, v_i)\right) \\
&\approx \sum_{i=1}^{12} b_i(s, t)\boldsymbol{\sigma}(u_i, v_i) = \sum_{i=1}^{12} b_i(s, t)\boldsymbol{x}_i^{(0)}. \tag{4.51}
\end{aligned}
$$

In the second step above, the function $\boldsymbol{\sigma}(u, v)$ is locally approximated as linear over the small domain region corresponding to S.

The displacement of a point on the middle surface in its Darboux frame is, by (4.1),

$$(\alpha, \beta, \gamma) = \left(\boldsymbol{\sigma}'(u, v) - \boldsymbol{\sigma}(u, v)\right)(\boldsymbol{t}_1, \boldsymbol{t}_2, \boldsymbol{n}). \tag{4.52}$$

Obtaining the Jacobian with entries $\frac{\partial s}{\partial u}$, $\frac{\partial s}{\partial v}$, $\frac{\partial t}{\partial u}$, and $\frac{\partial t}{\partial v}$ from (4.51), the strain energy of the shell can be integrated over each subdivision element of $\boldsymbol{\sigma}'$. For accuracy, all needed geometric invariants are nonetheless computed under the original parametrization $\boldsymbol{\sigma}$.

If the middle surface of a shell is not parametric but either free-form or described by an implicit equation, the subdivision surface $\boldsymbol{\sigma}'(u, v)$ for the deformed shape is subtended by a triangular mesh over the shell's 3-D range data before the deformation. Essentially, the original middle surface is approximated by $\boldsymbol{\sigma}'$ with the vertices at their pre-deformation positions $\boldsymbol{x}_i^{(0)}$.

Whether the shell is parametric or not, let m be the number of vertices of the subdivision surface $\boldsymbol{\sigma}'$. The deformed shape is characterized by the column vector $\boldsymbol{\Delta} = (\boldsymbol{\delta}_1^T, \ldots, \boldsymbol{\delta}_m^T)^T$, which consists of $3m$ coordinate variables. After the deformation, the vertices are at $\boldsymbol{x}_i = \boldsymbol{x}_i^{(0)} + \boldsymbol{\delta}_i$ for $1 \leq i \leq m$.

4.4.1 Stiffness Matrix

In the case of a small deformation, the system is linear following the linear elasticity theory and can be easily solved. We rewrite the strain energy U_ε in (4.34) into a matrix form:

$$U_\varepsilon = \boldsymbol{\Delta}^T K_s \boldsymbol{\Delta}, \qquad (4.53)$$

where K_s is the (symmetric) stiffness matrix constructed as follows. Assume there are N_e elements in the triangular control mesh of $\boldsymbol{\sigma}'$. Let S_k denote the kth element. Number the neighboring vertices locally so they are at $\boldsymbol{x}_1, \boldsymbol{x}_2, \cdots, \boldsymbol{x}_{12}$, respectively. The displacement field $(\alpha, \beta, \gamma)^T$ of S_k is decided by $\boldsymbol{\delta}_1^T, \ldots, \boldsymbol{\delta}_{12}^T$, where $\boldsymbol{\delta}_i = (\delta_{3(i-1)+1}, \delta_{3(i-1)+2}, \delta_{3(i-1)+3})^T$, for $1 \le i \le 12$. Each of α, β, γ is a linear combination of these 36 variables.

Next, we illustrate over the integral summand involving ϵ_1^2 in (4.34). By its definition (4.24), ϵ_1 is still a linear combination of these 36 variables, say, $\epsilon_1 = \sum_{l=1}^{36} N_l \delta_l$. Let $\boldsymbol{t}_1 = (t_{1x}, t_{1y}, t_{1z})^T$, $\boldsymbol{t}_2 = (t_{2x}, t_{2y}, t_{2z})^T$, and $\boldsymbol{n} = (n_x, n_y, n_z)^T$. The forms of N_ls are given as, for $1 \le i \le 12$,

$$
\begin{aligned}
N_{3(i-1)+1} &= \boldsymbol{t}_1[b_i t_{1x}] + (\nabla_{t_1} \boldsymbol{t}_2 \cdot \boldsymbol{t}_1) b_i t_{2x} + (\nabla_{t_1} \boldsymbol{n} \cdot \boldsymbol{t}_1) b_i n_x \\
&= \xi_1 \frac{\partial b_i}{\partial u} t_{1x} + \xi_1 b_i \frac{\partial t_{1x}}{\partial u} + \eta_1 \frac{\partial b_i}{\partial v} t_{1x} + \eta_1 b_i \frac{\partial t_{1x}}{\partial v} \\
&\quad + (\nabla_{t_1} \boldsymbol{t}_2 \cdot \boldsymbol{t}_1) b_i t_{2x} - \kappa_1 b_i n_x,
\end{aligned}
$$

$$
\begin{aligned}
N_{3(i-1)+2} &= \boldsymbol{t}_1[b_i t_{1y}] + (\nabla_{t_1} \boldsymbol{t}_2 \cdot \boldsymbol{t}_1) b_i t_{2y} + (\nabla_{t_1} \boldsymbol{n} \cdot \boldsymbol{t}_1) b_i n_y \\
&= \xi_1 \frac{\partial b_i}{\partial u} t_{1y} + \xi_1 b_i \frac{\partial t_{1y}}{\partial u} + \eta_1 \frac{\partial b_i}{\partial v} t_{1y} + \eta_1 b_i \frac{\partial t_{1y}}{\partial v} \\
&\quad + (\nabla_{t_1} \boldsymbol{t}_2 \cdot \boldsymbol{t}_1) b_i t_{2y} - \kappa_1 b_i n_y,
\end{aligned}
$$

$$
\begin{aligned}
N_{3(i-1)+3} &= \boldsymbol{t}_1[b_i t_{1z}] + (\nabla_{t_1} \boldsymbol{t}_2 \cdot \boldsymbol{t}_1) b_i t_{2z} + (\nabla_{t_1} \boldsymbol{n} \cdot \boldsymbol{t}_1) b_i n_z \\
&= \xi_1 \frac{\partial b_i}{\partial u} t_{1z} + \xi_1 b_i \frac{\partial t_{1z}}{\partial u} + \eta_1 \frac{\partial b_i}{\partial v} t_{1z} + \eta_1 b_i \frac{\partial t_{1z}}{\partial v} \\
&\quad + (\nabla_{t_1} \boldsymbol{t}_2 \cdot \boldsymbol{t}_1) b_i t_{2z} - \kappa_1 b_i n_z,
\end{aligned}
$$

where b_is are the subdivision basis functions, and (ξ_1, η_1) is from (3.9). From (4.34), the

element stiffness matrix $K^{\epsilon_1^2}$ is a 36×36 matrix (symmetric) with entries

$$K^{\epsilon_1^2}_{lp} = \frac{e}{2(1-\mu^2)} \int_{S_k} hN_lN_pd\mathcal{A}. \tag{4.54}$$

Similarly, we construct $K^{\epsilon_2^2}$, $K^{\epsilon_1\epsilon_2}$, K^{ω^2}, $K^{\zeta_1^2}$, $K^{\zeta_2^2}$, $K^{\zeta_1\zeta_2}$, and K^{τ^2}. The stiffness matrix for the element is

$$\begin{aligned} K_{S_k} &= K^{\epsilon_1^2} + K^{\epsilon_2^2} + K^{\epsilon_1\epsilon_2} + K^{\omega^2} \\ &\quad + K^{\zeta_1^2} + K^{\zeta_2^2} + K^{\zeta_1\zeta_2} + K^{\tau^2}. \end{aligned} \tag{4.55}$$

Now we need to assemble K_{S_k} into K_s ($3m \times 3m$ matrix). The local indices of the vertices in K_{S_k} are converted to the global indices. After adding rows and columns of zeros for all vertices not appearing in S_k, K_{S_k} is expanded to a new $3m \times 3m$ matrix K'_{S_k}. The global stiffness matrix sums up all element contributions:

$$K_s = \sum_{k=1}^{N_e} K'_{S_k}. \tag{4.56}$$

4.4.2 Minimization of Potential Energy

Denote by $\boldsymbol{q}(u,v)$ the load field, which does potential

$$U_q = \int_\sigma \boldsymbol{q}(u,v) \cdot \boldsymbol{\delta}(u,v)\, d\mathcal{A} = \boldsymbol{\Delta}^T Q, \tag{4.57}$$

where Q is the vector of all nodal forces. The total potential energy of a shell is

$$U = U_\varepsilon - U_q = \boldsymbol{\Delta}^T K_s \boldsymbol{\Delta} - \boldsymbol{\Delta}^T Q, \tag{4.58}$$

where the strain energy U_ε is given in (4.53).

To minimize U, a system of equations in $\boldsymbol{\Delta}$ can be derived by differentiating (4.58) with respect to the vector and setting all partial derivatives to zero:

$$2K_s\boldsymbol{\Delta} = Q. \tag{4.59}$$

The linear system (4.59) can be easily solved using Gaussian elimination or a sparse matrix method.

A large deformation is governed by the nonlinear elasticity theory. The strain energy U_ε in (4.49) no longer takes the quadratic form $\mathbf{\Delta}^T K_s \mathbf{\Delta}$, but rather a quartic form. Minimization of the total potential energy $U_\varepsilon - U_q$ is done iteratively. In the case of point contacts, a conical initial displacement field is placed around each contact point. Minimization over the radius of the deformed region sets the initial value of $\mathbf{\Delta}$. The conjugate gradient method is employed to improve on $\mathbf{\Delta}$, with the gradients evaluated numerically. Interpolation in the local neighborhood improves the computational efficiency. On a Dell Optiplex GX745 computer with 2.66GHz CPU and 3.00GB of RAM, it usually takes several minutes to obtain the solution compared with several seconds in the linear case.

4.4.3 Boundary Conditions

Boundary conditions are handled in the same way as described in (12) — the boundary displacements are determined only by vertices at most one edge away (including added artificial vertices just outside the domain). This is because of the local support within the subdivision scheme in Figure 4.5. For every boundary edge, one artificial vertex is introduced. As shown in Figure 5.4, vertex 4 is artificial and positioned at $\boldsymbol{\sigma}_4 = \boldsymbol{\sigma}_2 + \boldsymbol{\sigma}_3 - \boldsymbol{\sigma}_1$, where $\boldsymbol{\sigma}_1$, $\boldsymbol{\sigma}_2$, and $\boldsymbol{\sigma}_3$ are the positions of the vertices 1, 2, and 3 which form a triangle. Vertex 4 affects the geometry of the surface element which corresponds to the triangle. Under the clamped condition (displacements and rotations fixed), the displacements of the vertices on the boundary and their adjacent vertices, inside or outside, must be zero. Under the simply supported condition (displacements fixed and rotations free), the displacements of the vertices on the boundary must be zero, while those of the adjacent vertices inside and outside the boundary must be opposite to each other.
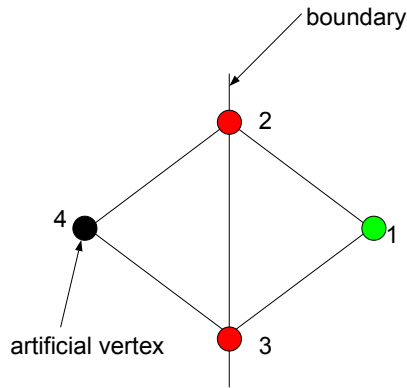
Figure 4.6 Clamped boundary condition, $\boldsymbol{\delta}_1 = \boldsymbol{\delta}_2 = \boldsymbol{\delta}_3 = \boldsymbol{\delta}_4 = 0$; simply supported boundary condition, $\boldsymbol{\delta}_2 = \boldsymbol{\delta}_3 = 0$, $\boldsymbol{\delta}_4 = -\boldsymbol{\delta}_1$.

4.5   Simulation

By default (except where specified otherwise), the metric system is used in our simulation and experiment. For instance, the unit of Young's modulus is Pa while the unit of length is meter. First, simulation tests under linear elasticity are conducted on a couple of bench mark problems, and the results are compared with their analytical solutions.[5] These problems in mechanics were designed to provide strict tests to deal with complex stress states.

4.5.1   Square Plate

The first bench mark problem involves a square plate under uniform load of gravity. Here, the effect of bending dominates those of elongation and shearing. As shown in Figure 4.7, the plate's boundary is clamped during the deformation.   Listed on the right are the values of the plate's length L, thickness h, Young's modulus E, and Poisson's ratio μ.

The maximum displacement at the center of the plate is $u_{\mathrm{max}} \approx 0.1376$ according to the analytical solution (80, p. 202), which is in the form of a trigonometric series. Figure 4.8 plots the computed maximum displacements normalized over u_{max} against the numbers of degrees of freedom. Note that every vertex in the control mesh has three degrees of freedom. The

---

[5]Closed-form solutions rarely exist for general thin shell problems.

$$L = 100.0$$
$$h = 1.0$$
$$E = 1.0 \cdot 10^7$$
$$\mu = 0.3$$
$$p = 1.0$$
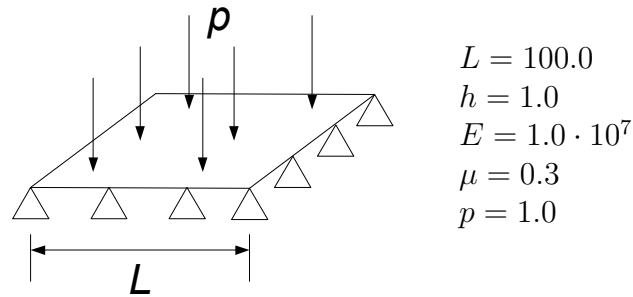
Figure 4.7   Plate under gravitational load and clamped at the boundary.

curve plot approaches the analytical value.[6]
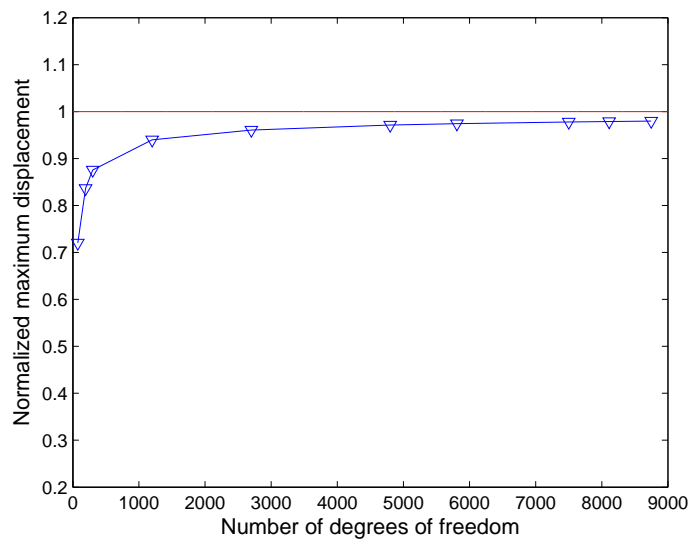
Figure 4.8   Convergence of the maximum displacement for the clamped plate in
Figure 4.7. The number of degrees of freedom equals three times the
number of vertices.

The geometry, load, and boundary condition are all symmetric in the example. The
Young's modulus and the load represent only a scaling factor and do not affect the overall
deformed shape. In Figure 4.9, the load p is scaled 200 times in order to illustrate the global

___

[6]The analytical solution considers bending only, whereas our formulation also incorporates in-plane extension, shearing and torsion, and is thus more realistic.

deformed shape. The added artificial vertices are drawn in red.
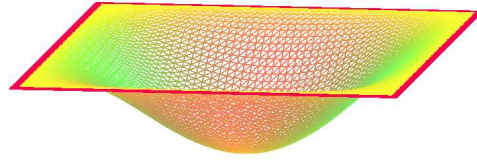
Figure 4.9   Calculated deformed shape (deflection scaled) for the clamped plate (artificial vertices marked red) in Figure 4.7.

4.5.2   Clamped Cylindrical Shell Panel

Next, we consider a cylindrical shell panel with the following geometric and material parameters and subjected to uniformly distributed transverse (normal to the surface) load p:

$$\alpha = 0.1 \text{rad.}, \qquad R = 100 \text{in.},$$

$$a = 20 \text{in.}, \qquad h = 0.125 \text{in.},$$

$$E = 0.45 \times 10^6 \text{psi}, \qquad \mu = 0.3, \qquad p = 0.04 \text{psi.}$$

As shown in Figure 4.10, this shell is clamped at its boundary.
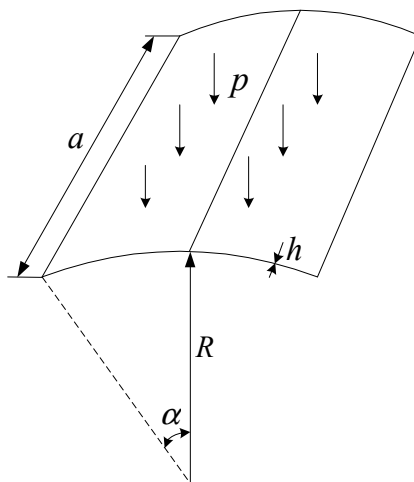
Figure 4.10   Clamped cylindrical shell panel under uniform transervers loads.

The vertical displacement at the center of the shell is 1.144×10^{-2}in. according to (59). Figure 4.11 plots the computed maximum displacements normalized over the reference value against the numbers of degrees of freedom. The curve approaches the reference value.
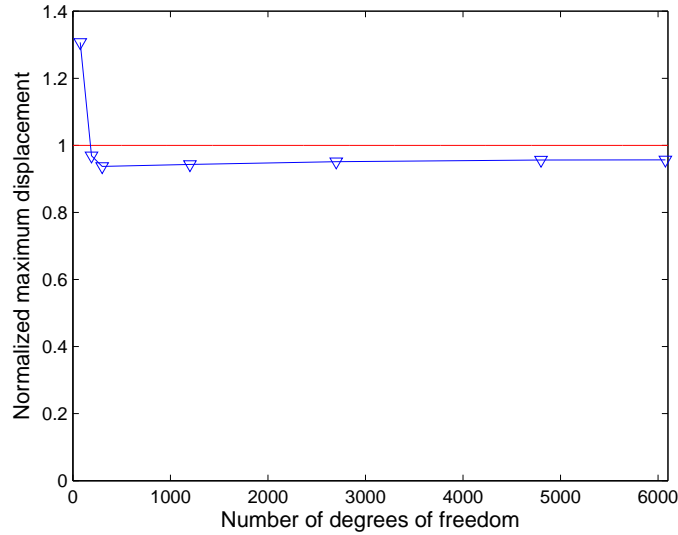
Figure 4.11   Convergence of the maximum displacement for the clamped cylindrical shell panel in Figure. 4.10.

4.5.3   Comparison with Commercial Packages

Shell elements in commercial packages usually fall into two categories: degenerated 3D solid elements and elements based on thick shell theories (especially the Reissner-Mindlin theory (39)).

A shell may be approximated as a collection of degenerated 3D solid elements, which are simple to formulate because their strains are approximated in Cartesian coordinates. Meanwhile, analysis of general curved shells uses curvilinear coordinates. Though this increases the complexity of derivation, the use of curvilinear coordinates provides increased accuracy, and is thus more preferable.

The Reissner-Mindlin theory allows for shearing throughout the thickness of a shell, and

best models thick shells (38). It requires C^0 interpolation only, simplifying the underlying basis functions, and is thus easy to implement. However, it often does not perform well in thin shell analysis because of shear and membrane locking.

We will compare our method with the use of shell elements S3 and T6. The element S3 is from the commercial software *ABAQUS* and based on the thick shell theory. Served as general-purpose shell element in *ABAQUS*, it is widely used in industry for both thin and thick shells. The element T6 is a degenerated 3D solid element from the SHELL93 library of another commercial package *ANSYS*.

Our performance criterion is accuracy in terms of the total number of degrees of freedom, which is standard in the FEM field. Here we use a well-known bench mark problem: a cylinder with rigid end diaphragms subjected to opposing normal point loads through its center (see Figure 4.12). The radius of the cylinder is $R = 300.0$. This problem tests the ability to model deformation caused by bending and membrane stresses. The analytical solution yields a displacement of 1.8248×10^{-5} under the load of $F = 1$ (67, p. 217). The results of using elements S3 and T6 are from (39).

$L = 600.0$
$R = 300.0$
$h = 3.0$
$E = 3.0 \cdot 10^6$
$\mu = 0.3$
$F = 1.0$
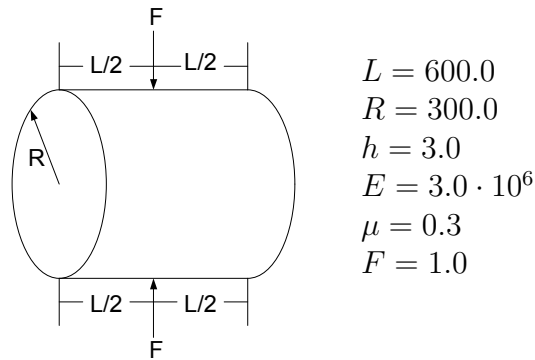
Figure 4.12   Pinched cylinder.

The convergence of our method to the analytical solution is shown in Figure 4.13, along with those of *ABAQUS* and *ANSYS*. The vertical axis represents the deflection at the point
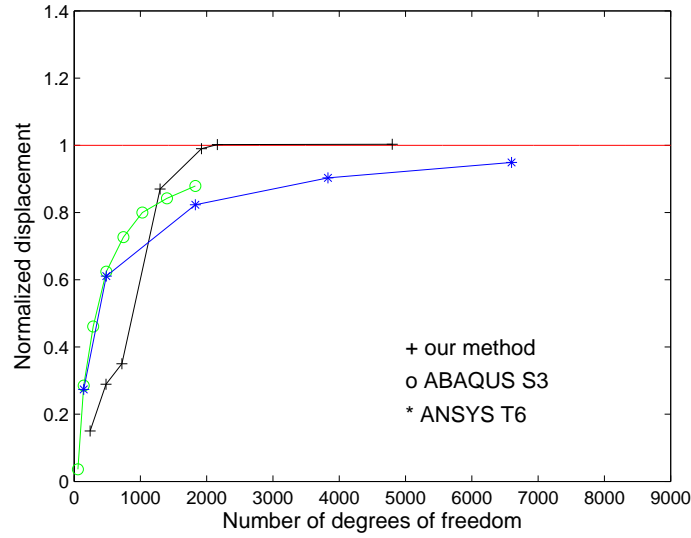
Figure 4.13 Convergence of the displacement under load for the pinched cylinder in Figure 4.12.

of contact normalized over the analytical displacement value. The normalized maximum displacement converges to 1 as the number of degrees of freedom increases, which means that the solutions converge to the analytical value.

To compare the rates of convergence of the three methods, denote by n the number of degrees of freedom in a finite element mesh, and by r the relative error. The relationship between r and n is perhaps best illustrated by plotting $\log(r)$ against $\log(n)$. If $r = n^p$, then $\log(r) = p \log(n)$, so the relationship between $\log(r)$ and $\log(n)$ is linear with the slope p. Therefore, the rate of convergence may be conveniently measured by the slope p. As shown in Figure 4.14, this slope of our method is approximately -2, which means the relative error decays roughly at the rate of $\frac{1}{n^2}$. In other words, the error r decreases by a factor of 4 with every doubling of the number of degrees of freedom n. In comparison, the relative errors of both S3 and T6 decay roughly at the rate of $\frac{1}{n}$. The convergence rate of our method is an order of magnitude higher than those of *ABAQUS* and *ANSYS*.[7]

---

[7]Although both S3 and T6 converge monotonically to the reference solution as reported in (39), T6 does so more slowly due to severe membrane locking.
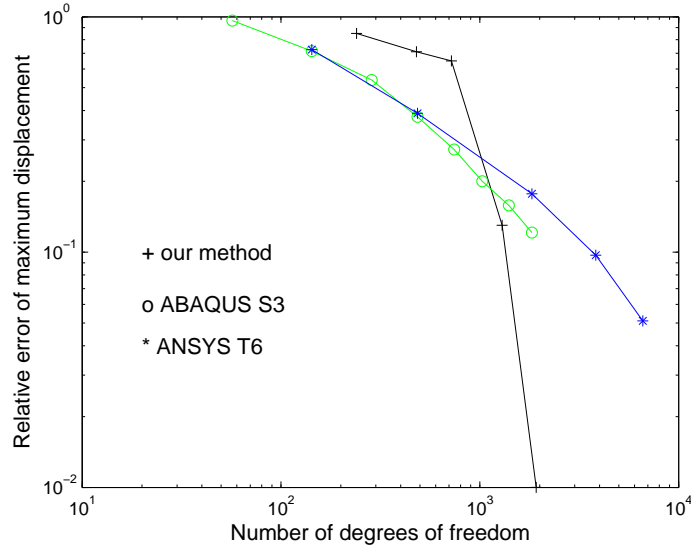
Figure 4.14   Rates of convergence.

4.5.4   Algebraic Surface

Simulation test under linear elasticity is also conducted on a monkey saddle. It is worthy of note that classical shell theory does not directly apply to the shape which does not have a known parametrization along the lines of curvature. The boundary condition requires that its edge is clamped during the deformation. The result generated by our method is shown in Figure 4.15. General mathematical surfaces, not easily modeled using the classical theory, are well in the application range of our method.

4.6   Experiment

The experimental setup (shown in Figure 4.16) includes an Adept Cobra 600 manipulator, a three-fingered BarrettHand, and a NextEngine's desktop 3-D scanner (accuracy 0.127mm). Every finger of the BarrettHand has a strain gauge sensor that measures contact force. To model point contact[8], a pin is mounted on each of the two grasping fingers. A triangular

---

[8]assumed between an object and a BarrettHand finger in this chapter.

$$x^3 - 3xy^2 = 5000z$$

$$(x, y) \in [-0.05, 0.05]$$
$$\times [-0.05, 0.05]$$

$$h = 0.001$$
$$E = 5.0 \cdot 10^6$$
$$\mu = 0$$
$$F = 1.0$$
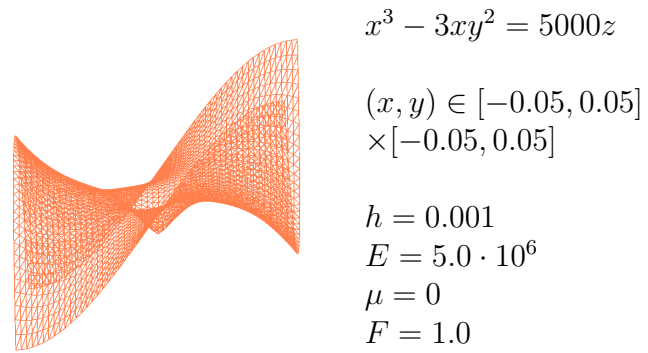
Figure 4.15   Deformations of a monkey saddle. The maximum displacement under point load is 0.019m.
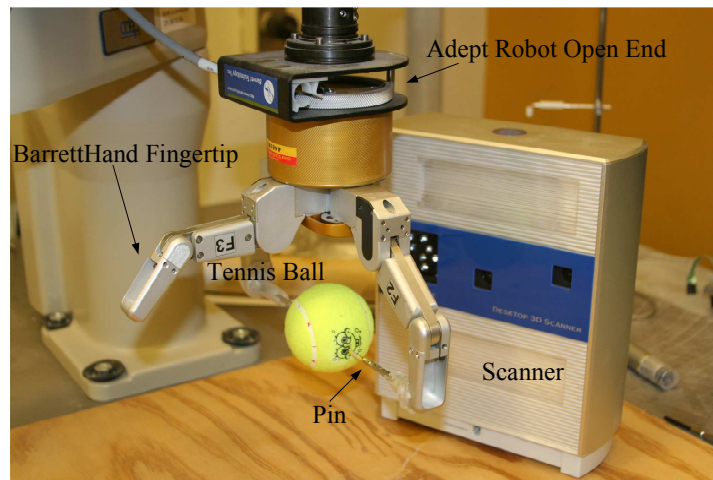
Figure 4.16   Experimental setup with a tennis ball.

mesh model of a deformed surface due to finger contact is generated by the scanner. We measure the modeling accuracy by matching the deformed surface from computation against the corresponding mesh model and averaging the distances from the mesh vertices to the deformed surface.[9]

4.6.1 Tennis Ball — Linear vs. Nonlinear Elasticities

For comparison, we have conducted an experiment on a tennis ball grasped at antipodal positions by the BarrettHand (see Figure 4.16). The rubber ball has an outer diameter of 65.0mm and thickness of 2.5mm. The Young's modulus of the rubber is approximated as 1MPa, and its Poisson's ratio approximated as 0.5. Two subdivision-based displacement fields, one for each finger contact, are used. Each field is defined over a 45mm $\times$ 45mm patch, which is large enough to describe the deformed area based on our observation.

The results are described in Table 4.1. In the table, each row corresponds to one instance of deformation. The first column in the table lists the force exerted by each finger. The second column (consisting of two subcolumns) lists the deformed shapes produced by the scanner. The third and fourth columns present the corresponding deformations computed according to the nonlinear and linear elasticity theories, respectively.

From the table, the nonlinear modeling results have smaller errors than the linear modeling results in three out of four rows, all corresponding to large deformations. In the first row, the two simulation results have comparable errors, which suggests that the deformation is within the range of linear elasticity. Starting from the second row, the two methods generate shapes that are visibly different from each other. In the second instance, the shape generated by the nonlinear method has an obvious dent comparable to the one on the real shape shown to the left, whereas the shape by the linear method to the right hardly shows any dent. We see that the

---

[9]We select a small underformed area on the computed surface by observation. Pick a vertex from the area, then place it at a vertex on the scanned mesh model. Align their normals, and rotate the small area to find the best match. Iterating over all vertices of the scanned mesh model will register the computed shape after deformation onto the scanned shape.
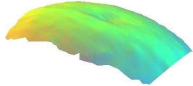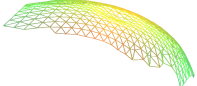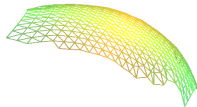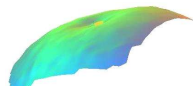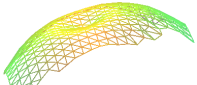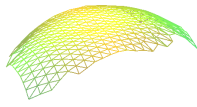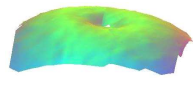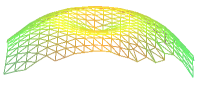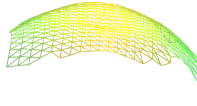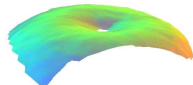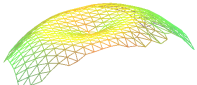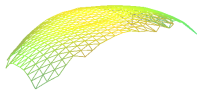
force (N)	scanned deformation		nonlinear deformation		linear deformation	
	shape	measured max disp. (mm)	shape	average error (mm)	shape	average error (mm)
10.63		2.56		0.31		0.30
16.50		6.05		0.62		0.85
20.37		9.12		0.81		2.0
21.48		10.27		0.65		2.37

Table 4.1   Comparisons between linear and nonlinear deformations on a tennis ball.

larger the force, the bigger the error of linear deformation. The error of nonlinear deformation does not increase with the force.

Grasping causes deformations in the regions around the contact while the rest of the surface hardly deforms. Figure 4.17 shows the deformed regions, under the finger force of 21.48N, superposed onto the scanned undeformed model of the tennis ball. The figure corresponds to the fourth instance in Table 4.1. The red curves, one at the top and the other at the bottom, mark the borders of these deformed regions. The measured maximum displacement of 10.27mm is achieved at two marked points. Due to symmetry, we only display the top deformed area. We see that the two antipodal contact points move closer under the force exerted by the two fingers. The scanned deformations on the tennis ball and the nonlinear results are within 7% of each other from the fourth instance in Table 4.1.
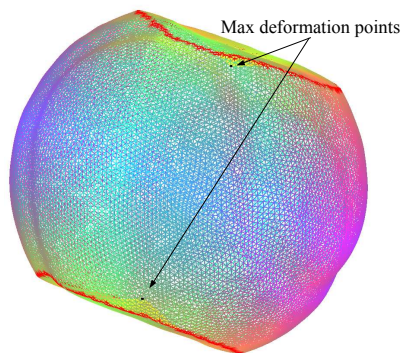

Max deformation points

Figure 4.17   Deformed tennis ball under grasping. The points in contact with the fingers have maximum displacements of 10.27mm.

4.6.2   Rubber Duck — Free-form Object

The surface of a real object usually has two varying principal curvatures. To demonstrate the ability to model free-form objects, we conduct an experiment on a rubber duck toy. The rubber has thickness 2.0mm. Its Young's modulus is approximated as 1MPa, and Poisson's ratio as 0.5.

Figure 4.18 displays the rear and the front views of the deformed rubber duck under an

antipodal grasp by the BarrettHand. The average modeling error is 0.58mm, which is within 7.4% of the scanned maximum displacement 8.56mm.
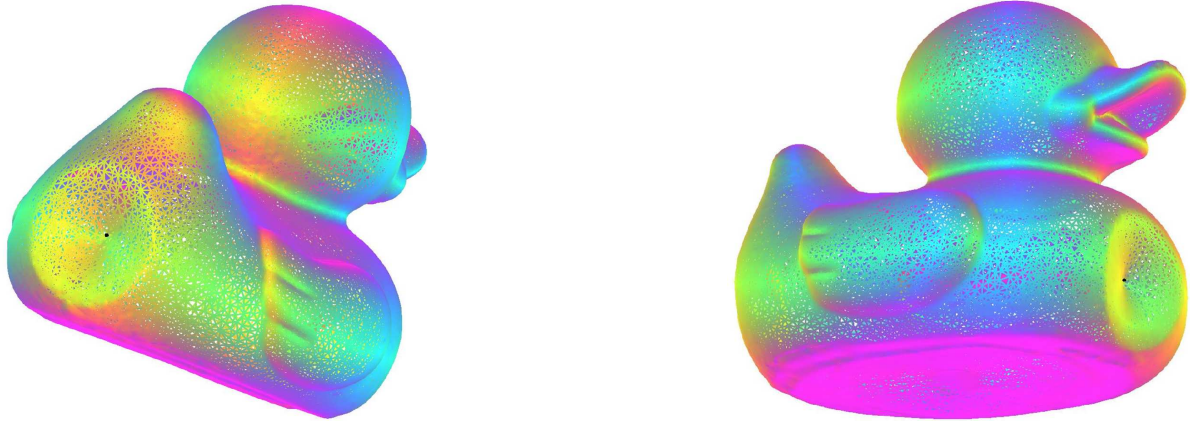

Figure 4.18 Deformed rubber duck under an antipodal grasp with force of 19.22N exerted by each finger. Two images show deformations from a rear view (left) and a front view (right) with maximum displacement (marked by dark points) of 8.56mm and 6.73mm, respectively.

4.7   Discussion

It is worth mentioning that our invariant-based formulation is mathematically equivalent to the tensor-based one in (28). However, ours provides much more clear geometric meanings to shell strains, which are buried in the latter formulation due to its complicated symbolism of tensor calculus.

In nonlinear modeling, an evolutionary algorithm rarely works due to its high dimensional search space. The conjugate gradient method improves the computational efficiency with a good initial guess obtained by interpolation over the local neighborhood.

Compared to commercial packages, our method achieves a higher convergence rate. Faster convergence rate implies a smaller number of mesh nodes needed, which in turn results in faster running time. The invariant-based formulation of thin shell strains increase accuracy and works with any parametrization. In contrast, commercial packages either approximate

strains in Cartesian coordinates, or use thick shell theory which could easily lead to shear and membrane locking when applied to thin shells.

There are two sources of errors in the simulation. The first is due to the discrepancy between the original surface $\boldsymbol{\sigma}(u, v)$ and its "deformed" shape $\boldsymbol{\sigma}'(u, v)$ as a subdivision surface under no deformation. This is because subdivision surfaces cannot represent some curved shapes exactly. The second source comes from modeling the deformation of the subdivision surface, a process that simplifies a variational problem (of finding a shape function satisfying Euler's equation) to that of determining a finite number of degrees of freedom.

In our experiment, several factors have affected the modeling accuracy: occlusion to the scanner, the scanner accuracy, and errors in the force readings (due to drifting of the zero points of the BarrettHand's strain gauge sensors). In the tennis ball experiment, the air pressure inside the ball also affects its deformation but is not modeled.

In a real situation, as the object deforms, the surface region in contact with the a robot finger usually grows larger and the load distribution changes. Modeling is expected to improve by considering area contacts and distributed loads. Installing tactile array sensors on the BarrettHand can dynamically estimate contact regions on the fingertips.

CHAPTER 5.   TOWARD TWO-FINGER GRASPING OF DEFORMABLE CURVE-LIKE OBJECTS

This chapter gives out a framework for two-finger squeeze grasp analysis. Two-finger grasping is widely used due to its simplicity and robustness. Point contacts with friction are considered. Modeling is based on the nonlinear elasticity theory, which is more accurate for large deformations compared with its linear counterpart. The evolution of contact friction cones could be characterized under the minimum potential energy criterion. Even if the two fingers were not initially placed at "graspable" positions, the contact friction cones may have rotated, resulting in an equilibrium grasp.

All objects addressed in this chapter are physically linear (governed by Hooke's law) but geometrically either linear or nonlinear. In the latter case, the linear elasticity theory is no more applicable. These objects are "closed curves" in the sense that their cross sections normal to the tangential direction are very small. For simplicity, we also assume that the physical property in the width direction is isotropic.

5.1   Grasp Modeling

Under external loads, an elastic curved object exhibits two principal behaviours: stretching and bending. Its deformation model is a lower dimensional analogue to the thin shell model in (36).

As shown in Figure 5.1, a thin curved object in our consideration is swept out by a constant cross section along a 2D closed curve $\boldsymbol{x}(u)$ referred to as the *middle curve*. The cross section

has width w and height h. This is essentially a degenerated shell with only one dominating dimension. To make physical sense, the curve is parametrized by arc length. Computation will easily carry over to arbitrary-speed curves.
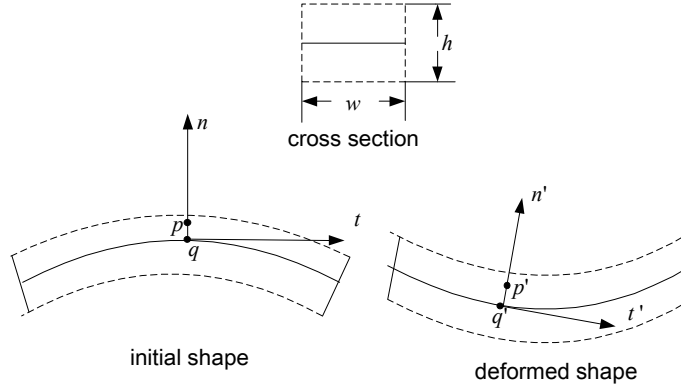

Figure 5.1   Deformation of a curved shape with rectangular cross section. The point p in the shape is along the direction of the normal n at the point q on the middle curve. Points p' and q' are their displaced locations.

We follow Kirchhoff's assumption that lines initially normal to the middle curve remain straight after deformation, do not change their lengths, and remain normal to the middle curve of the deformed geometry.

Every point p in the curved shape is along the normal direction of some point $\boldsymbol{q} = \boldsymbol{x}(u)$ on the middle curve. Let $\boldsymbol{t}$ and $\boldsymbol{n}$ be the unit tangent and normal at $\boldsymbol{q}$, respectively. We have $\boldsymbol{p} = \boldsymbol{q} + y\boldsymbol{n}$, where y is the signed distance from $\boldsymbol{q}$ to $\boldsymbol{p}$. The displacement $\boldsymbol{\delta}(u)$ of $\boldsymbol{q}$ is described as

$$\boldsymbol{\delta}(u) = \alpha(u)\boldsymbol{t} + \beta(u)\boldsymbol{n}. \tag{5.1}$$

Under a load, at the point $\boldsymbol{p}$, the extensional strain ϵ is

$$\epsilon = \boldsymbol{t}[\alpha] + (\nabla_t \boldsymbol{n} \cdot \boldsymbol{t})\beta = \alpha' - \kappa\beta, \tag{5.2}$$

where $\boldsymbol{t}[\alpha]$ is the *directional derivative* of α with respect to $\boldsymbol{t}$, and $\nabla_t \boldsymbol{n}$ is the *covariant derivative* which measures the rate of change of the normal $\boldsymbol{n}$ along the middle curve at $\boldsymbol{q}$. Denote

by ϕ the amount of rotation of the normal toward $\boldsymbol{t}$. We have

$$\phi = -\boldsymbol{t}[\beta] + (\nabla_t \boldsymbol{n} \cdot \boldsymbol{t})\alpha = -\beta' - \kappa\alpha. \tag{5.3}$$

The change in curvature, which accounts for the change rate of the angle ϕ along the direction $\boldsymbol{t}$, is

$$\zeta = \boldsymbol{t}[\phi] = -\beta'' - \kappa'\alpha - \kappa\alpha'. \tag{5.4}$$

Denote by σ the stress, and by ε the strain at any point. Let e be the modulus of elasticity, or Young's modulus. We have

$$\sigma = e(\epsilon + y\zeta),$$

$$\varepsilon = \epsilon + y\zeta.$$

Then the energy density is

$$dU_\epsilon = \frac{1}{2}\sigma\varepsilon dV = \frac{1}{2}e(\epsilon + y\zeta)^2 dV. \tag{5.5}$$

The strain energy can be obtained as follows.

$$\begin{aligned}
U_\epsilon &= \int_V dU_\epsilon \\
&= \frac{1}{2}\int_V e(\epsilon + y\zeta)^2 w dy ds \\
&= \frac{1}{2}ew \int_0^L \int_{-\frac{h}{2}}^{\frac{h}{2}} (\epsilon + y\zeta)^2 dy ds \\
&= \frac{1}{2}ew \int_0^L (h\epsilon^2 + \frac{h^3}{12}\zeta^2) ds.
\end{aligned} \tag{5.6}$$

The component linear in the thickness h represents the extensional energy, and the cubic component represents the bending energy. We cannot consider stretching only for a closed curve because it will always result in change in curvature (and bending) unless the curve is a line segment.

It is well known that large deformations need to be described by the nonlinear elasticity theory. In the following, we present a geometrically exact model expressed in terms of geometric invariants. This model characterizes large strains and deformations, and is transformed from the nonlinear shell theory (79).

First, we have the relative elongation of an infinitesimal line element starting at q as:

$$\bar{\varepsilon} = \epsilon + \frac{1}{2}(\epsilon^2 + \phi^2). \tag{5.7}$$

The following term characterizes the variation of the curvature of the middle curve along the tangential direction:

$$\bar{\zeta} = (1 + \epsilon)(\boldsymbol{t}[\phi] + (\nabla_t \boldsymbol{n} \cdot \boldsymbol{t})\epsilon) - \phi(\boldsymbol{t}[\epsilon] - (\nabla_t \boldsymbol{n} \cdot \boldsymbol{t})\phi). \tag{5.8}$$

where

$$
\begin{aligned}
\kappa_{11} &= \boldsymbol{t}[\phi] + (\nabla_t \boldsymbol{n} \cdot \boldsymbol{t})\epsilon \\
&= -\beta'' - \kappa'\alpha - 2\kappa\alpha' + \kappa^2\beta, \\
\kappa_{13} &= \boldsymbol{t}[\epsilon] - (\nabla_t \boldsymbol{n} \cdot \boldsymbol{t})\phi \\
&= \alpha'' - \kappa'\beta - 2\kappa\beta' - \kappa^2\alpha.
\end{aligned}
$$

Replacing the corresponding terms in (4.49), the strain energy is

$$\bar{U}_\epsilon = \frac{1}{2}ew \int_0^L (h\bar{\varepsilon}^2 + \frac{h^3}{12}\bar{\zeta}^2)ds. \tag{5.9}$$

In case of a small deformation, equation (5.9) is essentially the same to (5.6).

5.1.1 Discretization

Denote by U_q the potential of the external load. The total potential energy is

$$U = U_\epsilon - U_q.$$

The necessary condition for equilibrium is that the first variation δU is zero. Even in the simplified case of pure bending (i.e. $\epsilon = 0$), calculus of variations will set up a sixth order

differential equation that has little hope to be solved exactly. Discretizing the object into finite elements reduces the displacement from a continuous field to a discrete one, allowing the application of numerical techniques to the potential energy minimization.

The curvature term ζ_{11} in (5.9) has second order derivative of the displacement. In order to guarantee finite potential energy, the basis functions should be square integrable, and their first and second-order derivatives should also be square integrable. The cubic B-spline basis functions meet this requirement. It can be considered as the counterpart of the subdivision surface used in (79).

Let $u \in [0, 1]$, the four basis functions are

$$
\begin{aligned}
b_1 &= (-u^3 + 3u^2 - 3u + 1)/6, \\
b_2 &= (3u^3 - 6u^2 + 4)/6, \\
b_3 &= (-3u^3 + 3u^2 + 3u + 1)/6, \\
b_4 &= u^3/6.
\end{aligned}
$$

Figure 5.2 shows four consecutive points along the middle curve $x(u)$. The position of any

Figure 5.2   Discretization.

point $x(u)$ in the shade interval $[p_2, p_3]$ can be represented in terms of the positions of these two end points plus two neighboring control points as

$$
x(u) = b_1 p_1 + b_2 p_2 + b_3 p_3 + b_4 p_4. \tag{5.10}
$$

Its displacement is then a linear combination of the displacements δ_i of these control points:

$$
\delta(u) = b_1 \delta_1 + b_2 \delta_2 + b_3 \delta_3 + b_4 \delta_4. \tag{5.11}
$$

Obviously, any control point influences the domain $[-2.0, 2.0]$. As shown in Figure 5.3, the second-order derivative is continuous. In our implementation, both the geometry (5.10)

and the displacement field (5.11) are discreized using these cubic B-spline basis functions. This leads to the so-called *isoparametric* finite element, which is preferred in the FEM field.
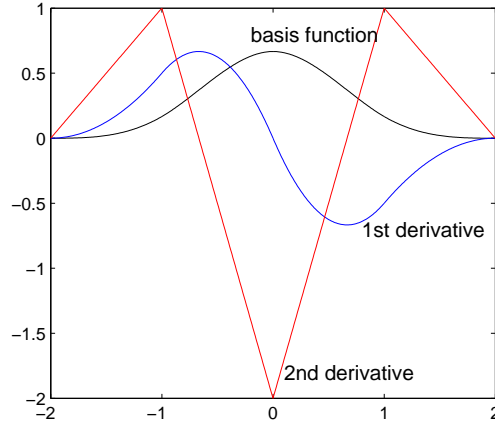

Figure 5.3 Concatenation of basis functions and the first and second-order derivatives.

5.1.2 Nonlinear Energy Minimization

We rewrite the strain energy U_ε in (5.9) into a matrix form:

$$U_\epsilon = \boldsymbol{\Delta}^T K_s \boldsymbol{\Delta}, \tag{5.12}$$

where $\boldsymbol{\Delta} = (\boldsymbol{\delta}_1^T, \ldots, \boldsymbol{\delta}_m^T)^T$, m is the number of control points, and K_s is the stiffness matrix.

Assume there are N elements in total. Let S_k denote the kth element. Number the neighboring points locally so they are at $\boldsymbol{x}_1, \cdots, \boldsymbol{x}_4$, respectively. The displacement field $(\alpha, \beta)^T$ of S_k is decided by $\boldsymbol{\delta}_1^T, \ldots, \boldsymbol{\delta}_4^T$, where $\boldsymbol{\delta}_i = (\delta_{2(i-1)+1}, \delta_{2(i-1)+2})^T$, for $1 \leq i \leq 4$. Both α and β are linear combinations of these 8 variables.

Next, we illustrate the computation of the strain energy (5.9) over the integral summand involving ε_{11}^2. Let $\boldsymbol{t} = (t_x, t_y)^T$, and $\boldsymbol{n} = (n_x, n_y)^T$. The forms of N_ls are given as, for

$1 \leq i \leq 4, 1 \leq j \leq 2,$

$$N_{2(i-1)+j} = (\frac{\partial b_i}{\partial u} t_q + b_i \frac{\partial t_q}{\partial u})(1 + \frac{1}{2}\epsilon - \frac{1}{2}\phi)$$
$$+ (\nabla_t \boldsymbol{n} \cdot \boldsymbol{t})b_i n_q (1 + \frac{1}{2}\epsilon + \frac{1}{2}\phi).$$

where q is x or y when $j = 1, 2$, respectively, and b_is are the basis functions. The element stiffness matrix $K^{\varepsilon_{11}^2}$ due to elongation is a 8×8 matrix with entries

$$K_{lp}^{\varepsilon_{11}^2} = \frac{1}{2}ew \int_{S_k} hN_l N_p ds. \tag{5.13}$$

Similarly, we construct the element matrix due to bending $K^{\zeta_{11}^2}$. The stiffness matrix for the element is

$$K_{S_k} = K^{\varepsilon_{11}^2} + K^{\zeta_{11}^2}.$$

We can assemble K_{S_k} into K_s by the standard procedure.

Denote by $\boldsymbol{q}(u)$ the load field, which has potential

$$U_q = \int_0^L \boldsymbol{q}(u) \cdot \boldsymbol{\delta}(u) \, ds = \boldsymbol{\Delta}^T Q, \tag{5.14}$$

where Q is the vector of all nodal forces. The total potential energy is

$$U = U_\epsilon - U_q = \boldsymbol{\Delta}^T K_s \boldsymbol{\Delta} - \boldsymbol{\Delta}^T Q, \tag{5.15}$$

where the strain energy U_ϵ is given in (5.9). The entries of K_s are functions of the unknown displacements. The nonlinear minimization of U is performed iteratively.

5.1.3 Boundary Condition

Boundary conditions are handled in a degenerate way compared with its thin shell counterpart described in (12). For a boundary vertex, one artificial vertex is introduced. The boundary conditions are shown in Figure 5.4. Vertex 3 is artificial and positioned at $\boldsymbol{x}_3 = 2\boldsymbol{x}_2 - \boldsymbol{x}_1$, where $\boldsymbol{x}_1$ and $\boldsymbol{x}_2$ are the positions of the vertices 1 and 2.
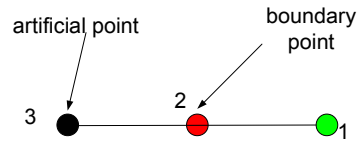
Figure 5.4   Displacement and rotation fixed, $\boldsymbol{\delta}_1 = \boldsymbol{\delta}_2 = \boldsymbol{\delta}_3 = 0$; displacement fixed and rotation free, $\boldsymbol{\delta}_2 = 0$, $\boldsymbol{\delta}_3 = -\boldsymbol{\delta}_1$; displacement and rotation free, $2\boldsymbol{\delta}_2 = \boldsymbol{\delta}_3 + \boldsymbol{\delta}_1$.

5.1.4   An Example

We proceed to show the effectiveness of our modeling technique by running a beam test case (68, p. 741). This example involves a straight beam ($E = 3 \cdot 10^7$psi) under uniformly distributed load. The beam is clamped at both ends. It has length 100.0in, width 1.0in, and height 1.0in.   Figure 5.5 plots the maximum deflection against the load. It shows that
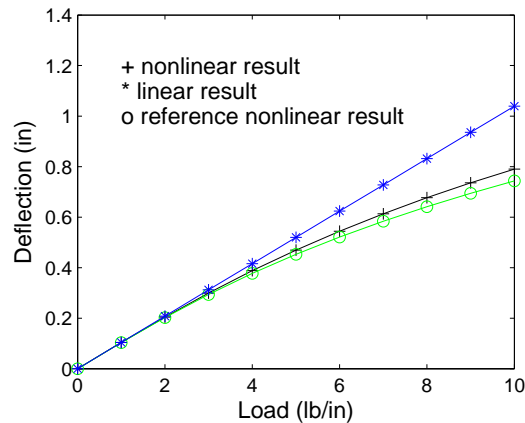

Figure 5.5   Beam under distributed load and clamped at both ends.

geometrically exact model provides a higher accuracy for large load.[1]

---

[1]The small difference between our nonlinear result and the reference one is because the latter considers bending only.

5.2 Grasp

A grasp of a rigid object achieves force closure if it can resist an arbitrary external wrench (force plus torque). Nguyen's (54) result on two-finger grasping under point contacts in the plane states that such a grasp is force-closure if the intersection of the two contact friction cones contains the line segment connecting the two contact points.

For deformable objects, *grasp analysis and synthesis are no longer purely geometric problems.* Due to the highly nonlinear nature of the potential energy form (5.15), determining the deformed shape analytically is difficult, if not impossible. This points us to start our investigation numerically to predict whether a grasp can be performed successfully.

We assume that deformation happens instantaneously such that the grasping forces do not vary during the process, and no velocity of the object has built up. It is common to ignore dynamics in modeling deformations using energy-based methods. Here it allows us to treat the grasping problem quasistatically. The outcome of a grasp on an object can then be determined based on the post-deformation geometry of the object and the original forces now applied at the current boundary locations. More precisely, *a pre-deformation finger placement is considered a grasp if the post-deformation finger placement would be force-closure on a rigid object with the same geometry as that of the deformed shape.*

Specifically, we consider a *squeeze grasp* $\mathcal{G}(u, v)$ with the two fingers positioned at $\boldsymbol{p} = \boldsymbol{x}(u)$ and $\boldsymbol{q} = \boldsymbol{x}(v)$ on the curve. As shown in Figure 5.6, we position $\boldsymbol{p}$ at the origin and $\boldsymbol{q}$ on the positive y-axis.

We assume that the bottom finger at $\boldsymbol{p}$ does not move while the top finger squeezes the curve toward $\boldsymbol{p}$ with a force of magnitude f. The effect will be equivalent to that generated by moving the two fingers toward each other, but this constraint on the lower finger is needed here for solution of the deformed shape. Note that the movement of the top finger is constrained to be on the y-axis. Slips between the fingers and the curve can happen during deformation when friction is not enough to prevent such motions from happening.
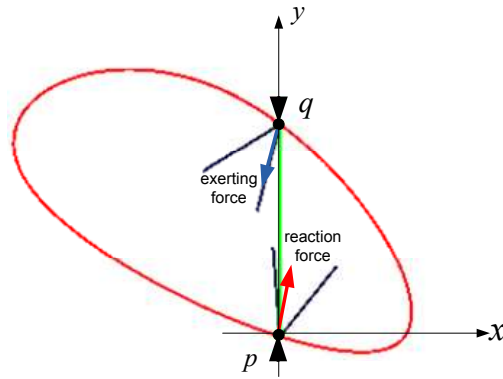
Figure 5.6   Grasping computation model. The displacement and rotation at contact point p are fixed, while point q can move freely.

The applied squeeze force at q must stay inside the friction cone. It points at p if the line segment $\overline{pq}$ is contained inside the cone. Otherwise it stays on the edge of the cone which forms a smaller angle with $\overline{pq}$. The reaction force exerted by the top finger at p can be computed after the deformation using FEM. It needs to stay inside the friction cone at p in the post-deformation state for the grasp to be achieved.

Under the above formulation, the deformation of the curve (and thus the success of the grasp) is completely determined by the magnitude f of force exerted by the upper finger. The force magnitude is *feasible* if it results in equilibrium of the curve in the post-deformation state.

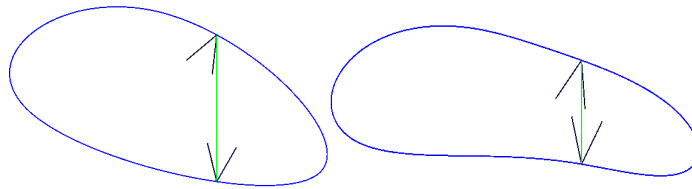Figure 5.7 shows the pre- and post-deformation states of a grasp.   The computation of the

Figure 5.7   A deformable grasp.

post-deformation will be detailed in Section 5.2.1. Here we note that the line segment connecting the two contact points was initially outside the top friction cone, but becomes inside

with the cone rotating counterclockwise under deformation. The original finger placement would not be a force-closure or even equilibrium grasp on a rigid object of the same shape.

5.2.1 Grasp Testing

In Figure 5.8, the finger contact points p and q are represented by points p_0 and q_0. Points p_{-1}, p_1, q_{-1} and q_1 are in the immediate neighborhood of points p_0 and q_0, respectively. Based on the boundary condition handling method described in Section 5.1.3, if we consider

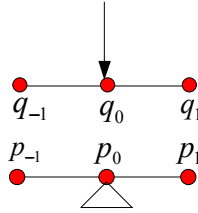Figure 5.8   Points near the finger contact points.

p_0 as a boundary point, p_{-1} and p_1 are artificial points to each other. Recall that δ represents the displacement at some point, we can formulate the constraints as

$$\delta_{-1} = \delta_0 = \delta_1 = 0. \tag{5.16}$$

They constrain the translation and rotation of the curve at p so that a unique FEM solution exists. These constraints indeed form a minimum set of conditions that must be satisfied in two dimensions for the computation.

In Figure 5.9, points p and q are initial contact positions. After deformation, q moves to q'. Since the top finger can only move along the y-axis toward the origin where the bottom finger is placed, the new top contact position is point q_1'. Finally, we check if the line segment connecting p and q_1' lies inside the two corresponding friction cones. The grasp is successful if so.
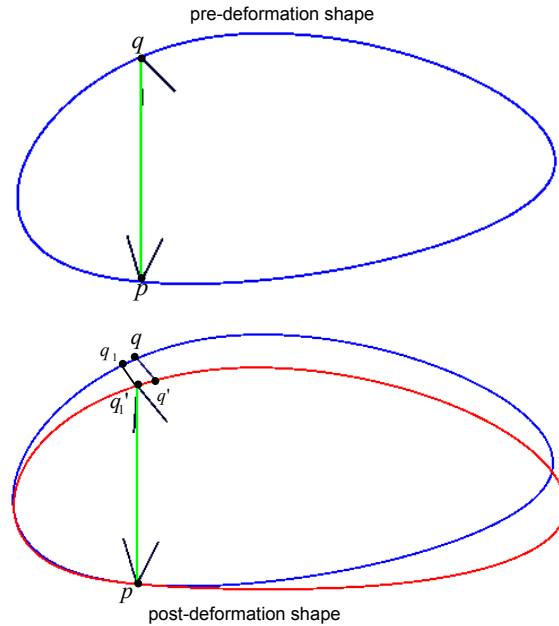
Figure 5.9 Quasi-static analysis. Points p and q are initial contact positions, whereas, points p and q'_1 are post-deformation ones.

5.2.2 Minimum Graspable Force Magnitude

Denote by $\mathcal{G}(u, v)$ a squeeze grasp as shown in Figure 5.6 with a finger placement at locations $p = x(u)$ and $q = x(v)$. A force of magnitude f exerted by the top finger is *feasible* if it results in a grasp. We can find a minimum force magnitude $f_{\min}$ such that the curve can be grasped as follows. Start with an initial value and double it at each step until the grasp is achieved or will not be so. (Observe the rotation of the top contact friction cone to determine it is toward the bottom contact friction cone.) Use bisection to find $f_{\min}$.

Table 5.1 lists three instances of grasping. The object has length 241.6mm, width 1.0mm, and height 1.0mm. The value of its Young's modulus is 100.0Pa. The value of the friction coefficient is 0.4. The first column in the table presents the initial configurations. The second column lists the results after deformations. The third column shows the minimum grasp force magnitudes. In the table, each row corresponds to one instance of grasping.

To determine the influence of Young's modulus on $f_{\min}$, we recall that the deformation
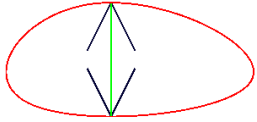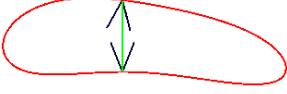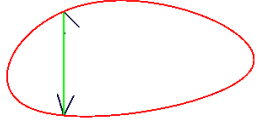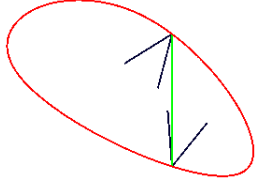
before grasping	after grasping	min grasping force
		$\sim 0N$
		0.2N
		0.5N

Table 5.1   Three grasps of a deformable object with two fingers.

computation is to minimize

$$\frac{1}{2}ew \int_0^L (h\varepsilon_{11}^2 + \frac{h^3}{12}\zeta_{11}^2)ds - \boldsymbol{f} \cdot \boldsymbol{\delta}.$$

If we change the value of Young's modulus from e to ce, the problem is equivalent to minimize

$$c\left(\frac{1}{2}ew \int_0^L (h\varepsilon_{11}^2 + \frac{h^3}{12}\zeta_{11}^2)ds - \frac{\boldsymbol{f}}{c} \cdot \boldsymbol{\delta}\right).$$

This implies that Young's Modulus is a scaling factor. the minimum grasp force magnitude for the value ce of Young's Modulus is $cf_{\min}$.

5.2.3   Prolonged Graspable Segment

A grasp $\mathcal{G}(u,v)$ at locations $\boldsymbol{x}(u)$ and $\boldsymbol{x}(v)$ of a curve $\boldsymbol{x}$ is achievable if the set of feasible grasping forces for the finger placement is nonempty. A domain interval $[v_l, v_r]$ of the curve defines a *graspable boundary segment* for $\boldsymbol{p} = \boldsymbol{x}(u)$ if every grasp $\mathcal{G}(u,v)$, $v \in [v_l, v_r]$ is achievable. For a rigid object, finding such an interval depends only on local geometry, and the computation is straightforward.

Figure 5.10 shows grasps of a deformable object and of a rigid one with the same shape. For the purpose of comparison, the deformable object is drawn in its original shape and coincides with the rigid object. One finger is fixed at p in all the grasps. The arc $\widehat{d_l d_r}$ represents the segment of feasible locations where the top finger can be positioned to grasp the deformable object, while the arc $\widehat{s_l s_r}$ represents the segment for the rigid object. The graspable segment is enlarged on the deformable object due to the change in contact geometry. Generally, deformation helps grasping.
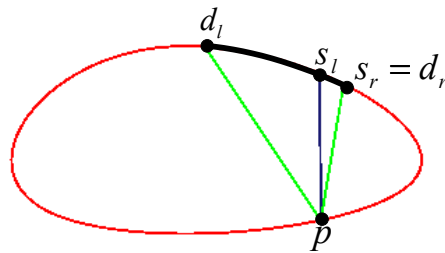

Figure 5.10   Increased graspable segments. The arc $\widehat{d_l d_r}$ is for the deformable object, and the arc $\widehat{s_l s_r}$ is for the rigid one.

5.2.4   Disturbance

Robustness of a grasp of a deformable object has different implications than that of a rigid one. In the latter case, every finger can exert a force of any magnitude inside the contact friction cone for a non-empty null space of the grasp matrix. Equivalently, an arbitrary disturbance force can be resisted. In contrast, the magnitude of a disturbance force applied to a grasped deformable object is bounded. Otherwise, the grasp will be broken.

To illustrate the above, consider an object grasped by two fingers. An exerted disturbance force will result in reaction forces at the two finger contacts, which can be determined after the respective displacements are computed under, say, the linear elasticity model. At each finger contact, this reaction force is combined with the original grasping force. The composite force must lie inside the corresponding contact friction cone.
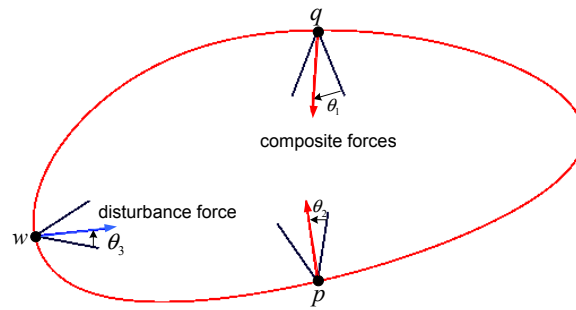
Figure 5.11   Disturbance model. Points p and q are the finger contacts. Point w is the disturbance contact.

As shown in Figure 5.11, an object is grasped at points p and q. It has the same mechanical properties as the one in Table 5.1. A disturbance force is now applied at the point w. It lies inside the friction cone $\mathcal{C}$ at the point of application. Denote by θ_i the angle between the force direction and one edge of the friction cones. Figure 5.12 shows that the composite finger forces at p and q change their directions as the disturbance force varies from one edge to the other of the friction cone $\mathcal{C}$. During the change, the magnitude of the disturbance force stays constant.
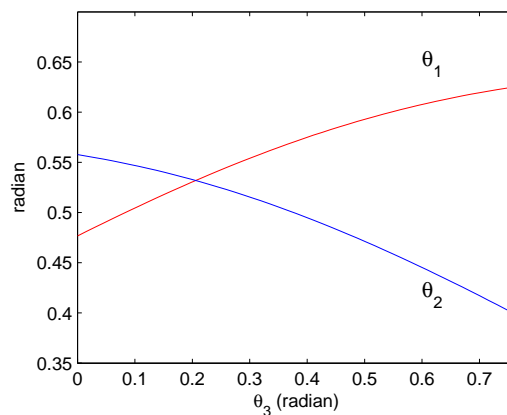

Figure 5.12   Evolution of the finger force directions θ_1 and θ_2 to maintain the grasp in reaction to the change in the direction of the disturbance force from 0 to 0.76 (radian) while the magnitude of the disturbance force stays constant.

In Figure 5.13, the direction of the disturbance force is fixed but its magnitude increases.

Both θ_1 and θ_2 will exceed $2\tan^{-1}(\mu)$. The grasp is broken when θ_1 first does so.
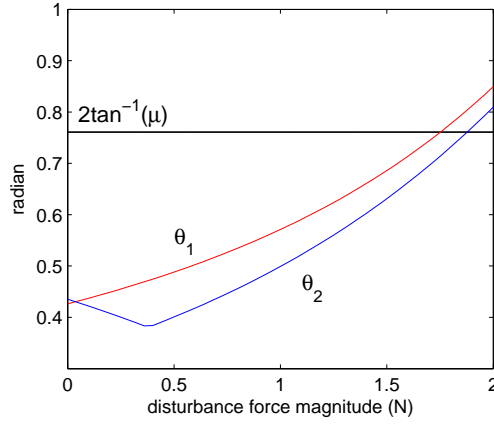
Figure 5.13 Evolution of θ_1 and θ_2 as a result of varying disturbance force magnitude with the disturbance force's direction unchanged.

5.3 Pure Bending of a Closed Curve

In real world, there is one physical response known as inextensional bending such that the membrane strain tends to vanish. In this section, solutions for pure bending of a closed curve will be presented.

As shown in Figure 5.14, a curve parametrized by arc length s is fixed at $s = s_1$. A force of magnitude f is exerted at $s = 0$ in the positive direction of x-axis. In this section, a calculus of variation solution will be presented.[2]

5.3.1 Pure Bending

If we consider bending only, extensional strain is zero everywhere

$$\alpha' - \kappa\beta = 0. \tag{5.17}$$

We can immediately get

$$\alpha' = \kappa\beta,$$

---

[2]provided by my thesis advisor Yan-Bin Jia.

Figure 5.14 A curve fixed at $s = s_1$ and squeezed at $s = 0$ toward the positive direction of x-axis.

$$\beta = \frac{\alpha'}{\kappa}.$$

Therefore, the derivatives of β can be represented in terms of α as:

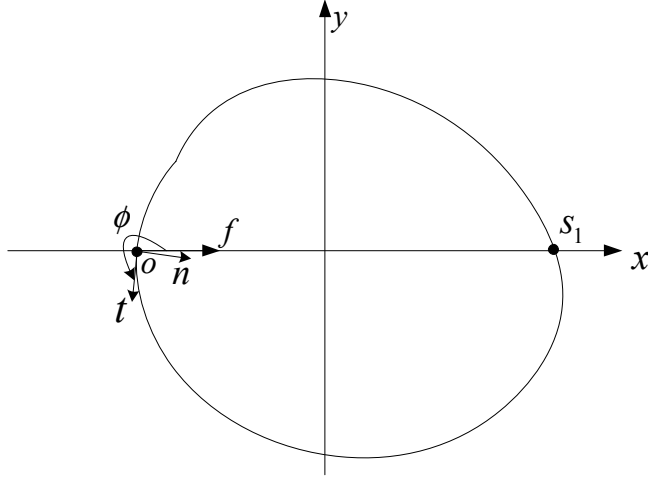$$\beta' = \frac{\alpha''}{\kappa} - \frac{\kappa'}{\kappa^2}\alpha',$$

$$\begin{aligned}
\beta'' &= \frac{\alpha'''}{\kappa} - \frac{\kappa'}{\kappa^2}\alpha'' - \frac{\kappa'}{\kappa^2}\alpha'' - (\frac{\kappa''}{\kappa^2} - 2\frac{\kappa'^2}{\kappa^3})\alpha' \\
&= \frac{\alpha'''}{\kappa} - 2\frac{\kappa'}{\kappa^2}\alpha'' + (2\frac{\kappa'^2}{\kappa^3} - \frac{\kappa''}{\kappa^2})\alpha'.
\end{aligned}$$

Substituting them into (5.4):

$$\begin{aligned}
\zeta &= -\beta'' - \kappa'\alpha - \kappa\alpha' \\
&= -\kappa'\alpha - (\kappa + 2\frac{\kappa'^2}{\kappa^3} - \frac{\kappa''}{\kappa^2})\alpha' + 2\frac{\kappa'}{\kappa^2}\alpha'' - \frac{\alpha'''}{\kappa}.
\end{aligned}$$

Obviously, ζ is a function of α and its first three derivatives. Subsequently, the strain energy is

$$U_\epsilon = \frac{ewh^3}{24} \int_0^L H(\alpha, \alpha', \alpha'', \alpha''')ds,$$

where $H = \zeta^2$, e is Young's modulus, w and h are the width and height of the curve's cross section, respectively.

In the case of a circle with radius r, $\kappa = \frac{1}{r}$. We have

$$\zeta = -\frac{\alpha'}{r} - r\alpha'''.$$

5.3.2 Boundary Conditions

The point s_1 does not move means that

$$\alpha(s_1) = 0, \tag{5.18}$$

and

$$\beta(s_1) = 0. \tag{5.19}$$

For bending only, equation (5.19) is equal to

$$\alpha'(s_1) = 0. \tag{5.20}$$

At the same time, the post-deformation shape of the curve should be closed, therefore

$$\alpha(0) = \alpha(L), \tag{5.21}$$

$$\beta(0) = \beta(L). \tag{5.22}$$

Equation (5.22) also means:

$$\alpha'(0) = \alpha'(L). \tag{5.23}$$

We also require that the curve after deformation has continuous tangent at $s = 0$. Denote by $\boldsymbol{x}(s)$ a unit-speed curve before the deformation. After the deformation, it becomes

$$\boldsymbol{x}(s) + \alpha\boldsymbol{t} + \beta\boldsymbol{n}$$

with new tangent

$$(1 + \alpha' - \kappa\beta)\boldsymbol{t} + (\kappa\alpha + \beta')\boldsymbol{n} = \boldsymbol{t} + (\kappa\alpha + \beta')\boldsymbol{n}.$$

Because α, α' and β already have equal values at $s = 0$ and $s = L$, we only need to exert the constraint $\beta'(0) = \beta'(L)$. Differentiating equation (5.17) leads to

$$\alpha'' - \kappa'\beta + \kappa\beta' = 0.$$

Subsequently, it is equivalent to exert the constraint

$$\alpha''(0) = \alpha''(L).$$

5.3.3 Variational Solution

The load potential is

$$W = f(\alpha(0)cos\phi - \beta(0)sin\phi) \tag{5.24}$$

$$= f(\alpha(0)cos\phi - \frac{\alpha'(0)}{\kappa(0)}sin\phi). \tag{5.25}$$

Then the potential energy is

$$U = \tilde{E}\int_0^L H(\alpha, \alpha', \alpha'', \alpha''')ds - f(\alpha(0)cos\phi - \frac{\alpha'(0)}{\kappa(0)}sin\phi). \tag{5.26}$$

Since there are five constraints, we consider variation

$$\alpha + \varepsilon_1\eta_1 + \varepsilon_2\eta_2 + \varepsilon_3\eta_3 + \varepsilon_4\eta_4 + \varepsilon_5\eta_5 + \varepsilon_6\eta_6,$$

where η_is, for $1 \leq i \leq 6$, are arbitrary functions. To satisfy the constraints, we must have

$$J_1(\varepsilon_1, \varepsilon_2, \varepsilon_3, \varepsilon_4, \varepsilon_5, \varepsilon_6) \equiv \sum_{i=1}^5 \varepsilon_i\eta_i(s_1) = 0, \tag{5.27}$$

$$J_2(\varepsilon_1, \varepsilon_2, \varepsilon_3, \varepsilon_4, \varepsilon_5, \varepsilon_6) \equiv \sum_{i=1}^5 \varepsilon_i\eta_i'(s_1) = 0, \tag{5.28}$$

$$J_3(\varepsilon_1, \varepsilon_2, \varepsilon_3, \varepsilon_4, \varepsilon_5, \varepsilon_6) \equiv \sum_{i=1}^5 \varepsilon_i(\eta_i(L) - \eta_i(0)) = 0, \tag{5.29}$$

$$J_4(\varepsilon_1, \varepsilon_2, \varepsilon_3, \varepsilon_4, \varepsilon_5, \varepsilon_6) \equiv \sum_{i=1}^5 \varepsilon_i(\eta_i'(L) - \eta_i'(0)) = 0, \tag{5.30}$$

$$J_5(\varepsilon_1, \varepsilon_2, \varepsilon_3, \varepsilon_4, \varepsilon_5, \varepsilon_6) \equiv \sum_{i=1}^{5} \varepsilon_i(\eta_i''(L) - \eta_i''(0)) = 0. \tag{5.31}$$

Replace the α related terms in (5.26) with $\alpha + \varepsilon_1\eta_1 + \varepsilon_2\eta_2 + \varepsilon_3\eta_3 + \varepsilon_4\eta_4 + \varepsilon_5\eta_5 + \varepsilon_6\eta_6$. Let

$$U^*(\varepsilon_1, \varepsilon_2, \varepsilon_3, \varepsilon_4, \varepsilon_5, \varepsilon_6) \equiv U(\varepsilon_1, \varepsilon_2, \varepsilon_3, \varepsilon_4, \varepsilon_5, \varepsilon_6) + \sum_{i=1}^{5} \lambda_i J_i(\varepsilon_1, \varepsilon_2, \varepsilon_3, \varepsilon_4, \varepsilon_5, \varepsilon_6). \tag{5.32}$$

Since U^* achieves an extremum at $\varepsilon_1 = \varepsilon_2 = \varepsilon_3 = \varepsilon_4 = \varepsilon_5 = \varepsilon_6 = 0$, its partial derivatives with respect to ε_is, for $1 \le i \le 6$, must all vanish.

$$
\begin{aligned}
\frac{\partial U^*}{\partial \varepsilon_i}\Big|_{\varepsilon_i=0} = {} & \tilde{E}\int_0^L (H_\alpha - \frac{dH_{\alpha'}}{ds} + \frac{d^2H_{\alpha''}}{ds^2} - \frac{d^3H_{\alpha'''}}{ds^3})\eta_i ds \\
& + \tilde{E}(H_{\alpha'} - \frac{dH_{\alpha''}}{ds} + \frac{d^2H_{\alpha'''}}{ds^2})\eta_i|_0^L + \tilde{E}(H_{\alpha''} - \frac{dH_{\alpha'''}}{ds})\eta_i'|_0^L + \tilde{E}H_{\alpha'''}\eta_i''|_0^L \\
& - f\cos\phi\eta_i(0) + f\frac{\sin\phi}{\kappa(0)}\eta_i'(0) + \lambda_1\eta_i(s_1) + \lambda_2\eta_i'(s_1) + \lambda_3\eta_i|_0^L + \lambda_4\eta_i'|_0^L + \lambda_5\eta_i''|_0^L.
\end{aligned}
$$

Merging terms with the same factors leads to:

$$
\begin{aligned}
\frac{\partial U^*}{\partial \varepsilon_i}\Big|_{\varepsilon_i=0} = {} & \tilde{E}\int_0^L (H_\alpha - \frac{dH_{\alpha'}}{ds} + \frac{d^2H_{\alpha''}}{ds^2} - \frac{d^3H_{\alpha'''}}{ds^3})\eta_i ds \\
& + (\tilde{E}(H_{\alpha'} - \frac{dH_{\alpha''}}{ds} + \frac{d^2H_{\alpha'''}}{ds^2}) + \lambda_3)\eta_i|_0^L - f\cos\phi\eta_i(0) \\
& + (\tilde{E}(H_{\alpha''} - \frac{dH_{\alpha'''}}{ds}) + \lambda_4)\eta_i'|_0^L + f\frac{\sin\phi}{\kappa(0)}\eta_i'(0) \\
& + (\tilde{E}H_{\alpha'''} + \lambda_5)\eta_i''|_0^L + \lambda_1\eta_i(s_1) + \lambda_2\eta_i'(s_1).
\end{aligned}
$$

Then we easily set $\lambda_1 = \lambda_2$ to eliminate the two terms involving s_1:

$$
\begin{aligned}
\frac{\partial U^*}{\partial \varepsilon_i}\Big|_{\varepsilon_i=0} = {} & \tilde{E}\int_0^L (H_\alpha - \frac{dH_{\alpha'}}{ds} + \frac{d^2H_{\alpha''}}{ds^2} - \frac{d^3H_{\alpha'''}}{ds^3})\eta_i ds \\
& + (\tilde{E}(H_{\alpha'} - \frac{dH_{\alpha''}}{ds} + \frac{d^2H_{\alpha'''}}{ds^2}) + \lambda_3)\eta_i|_0^L - f\cos\phi\eta_i(0) \\
& + (\tilde{E}(H_{\alpha''} - \frac{dH_{\alpha'''}}{ds}) + \lambda_4)\eta_i'|_0^L + f\frac{\sin\phi}{\kappa(0)}\eta_i'(0) \\
& + (\tilde{E}H_{\alpha'''} + \lambda_5)\eta_i''|_0^L.
\end{aligned}
$$

Theorem 2. *Euler's equation must be satisfied:* $G \equiv H_\alpha - \frac{dH_{\alpha'}}{ds} + \frac{d^2H_{\alpha''}}{ds^2} - \frac{d^3H_{\alpha'''}}{ds^3} = 0.$

Proof. We first show that $G = 0$ at $s \ne 0, L$ by contradiction. First, we assume that $G > 0$ at some s without losing generality. Then there exists some $\varepsilon > 0$ such that $G \ne 0$ over

$(s - \varepsilon, s + \varepsilon)$. We can make ε small enough such that $0, L \notin (s - \varepsilon, s + \varepsilon)$. Now construct a function η_i such that $\eta_i(t) > 0$ over $(s - \varepsilon, s + \varepsilon)$ and $\eta_i(t) = 0$ at other points in $[0, L]$. By contradiction it follows that

$$\eta_i(0) = \eta_i(L) = \eta_i'(0) = \eta_i'(L) = \eta_i''(0) = \eta_i''(L) = 0.$$

The partial derivative reduces to

$$\frac{\partial U^*}{\partial \varepsilon_i}\Big|_{\varepsilon_i = 0} = \tilde{E} \int_0^L (H_\alpha - \frac{dH_{\alpha'}}{ds} + \frac{d^2 H_{\alpha''}}{ds^2} - \frac{d^3 H_{\alpha'''}}{ds^3}) \eta_i \, ds > 0.$$

Hence a contradiction.

By continuity, $G = 0$ must also hold at $s = 0, L$. $\qquad\qquad\square$

The partial derivative further reduces to

$$
\begin{aligned}
\frac{\partial U^*}{\partial \varepsilon_i}\Big|_{\varepsilon_i = 0} &= (\tilde{E}(H_{\alpha'} - \frac{dH_{\alpha''}}{ds} + \frac{d^2 H_{\alpha'''}}{ds^2}) + \lambda_3)\eta_i|_0^L - f\cos\phi\,\eta_i(0) \\
&+ (\tilde{E}(H_{\alpha''} - \frac{dH_{\alpha'''}}{ds}) + \lambda_4)\eta_i'|_0^L + f\frac{\sin\phi}{\kappa(0)}\eta_i'(0) + (\tilde{E}H_{\alpha'''} + \lambda_5)\eta_i''|_0^L.
\end{aligned}
$$

Now we let $\eta_i(s) = C \neq 0$ be a constant function. All derivatives vanish, resulting in

$$(\tilde{E}(H_{\alpha'} - \frac{dH_{\alpha''}}{ds} + \frac{d^2 H_{\alpha'''}}{ds^2}) + \lambda_3)|_0^L C - f\cos\phi\,C = 0.$$

The two terms involving λ_3 cancel each other, yielding

$$(H_{\alpha'} - \frac{dH_{\alpha''}}{ds} + \frac{d^2 H_{\alpha'''}}{ds^2})|_0^L = \frac{f\cos\phi}{\tilde{E}}.$$

Similarly, we let $\eta_i(s) = \sin\frac{2\pi s}{L}$ with its values and second derivatives vanishing at $s = 0, L$. We end up with the equation

$$(\tilde{E}(H_{\alpha''} - \frac{dH_{\alpha'''}}{ds}) + \lambda_4)|_0^L \frac{2\pi}{L} + f\frac{\sin\phi}{\kappa(0)}\frac{2\pi}{L} = 0.$$

Again, λ_4 gets eliminated, yielding

$$(H_{\alpha''} - \frac{dH_{\alpha'''}}{ds})|_0^L = -f\frac{\sin\phi}{\tilde{E}\kappa(0)}.$$

Finally, we choose $\eta_i(s) = cos\frac{2\pi s}{L}$. Then all first derivative terms disappear. The first two terms involving $\eta_i(0)$ and $\eta_i(L)$ cancel each other because $\eta_i(0) = \eta_i(L)$ and

$$(H_{\alpha'} - \frac{dH_{\alpha''}}{ds} + \frac{d^2 H_{\alpha'''}}{ds^2})|_0^L = \frac{f cos\phi}{\tilde{E}}.$$

Hence we have

$$H_{\alpha'''}|_0^L = 0.$$

To summarize, the curve after deformation satisfies the differential equation

$$H_\alpha - \frac{dH_{\alpha'}}{ds} + \frac{d^2 H_{\alpha''}}{ds^2} - \frac{d^3 H_{\alpha'''}}{ds^3} = 0 \tag{5.33}$$

subject to the following constraints

$$(H_{\alpha'} - \frac{dH_{\alpha''}}{ds} + \frac{d^2 H_{\alpha'''}}{ds^2})|_0^L = \frac{f cos\phi}{\tilde{E}}, \tag{5.34}$$

$$(H_{\alpha''} - \frac{dH_{\alpha'''}}{ds})|_0^L = -f\frac{sin\phi}{\tilde{E}\kappa(0)}, \tag{5.35}$$

$$H_{\alpha'''}|_0^L = 0, \tag{5.36}$$

$$\alpha|_0^L = 0, \tag{5.37}$$

$$\alpha'|_0^L = 0, \tag{5.38}$$

$$\alpha''|_0^L = 0, \tag{5.39}$$

$$\alpha(s_1) = 0, \tag{5.40}$$

$$\alpha'(s_1) = 0. \tag{5.41}$$

5.3.4   Unit Circle

Consider a unit circle under the applied force at its leftmost point in the direction of the positive x-axis. In this case,

$$\phi = \frac{3\pi}{2},$$

$$L = 2\pi,$$

$$s_1 = \pi,$$

$$H = (\alpha' + \alpha''')^2,$$

$$H_{\alpha'} = H_{\alpha'''} = 2(\alpha' + \alpha'''),$$

$$H_\alpha = H_{\alpha''} = 0.$$

The differential equation and boundary conditions are simplified with substitution of the above expressions.

$$\alpha'' + 2\alpha^{(4)} + \alpha^{(6)} = 0. \tag{5.42}$$

subject to

$$\alpha' + 2\alpha''' + \alpha^{(5)}\big|_0^{2\pi} = 0, \tag{5.43}$$

$$\alpha'' + \alpha^{(4)}\big|_0^{2\pi} = -\frac{f}{2\tilde{E}}, \tag{5.44}$$

$$\alpha' + \alpha'''\big|_0^{2\pi} = 0, \tag{5.45}$$

$$\alpha\big|_0^{2\pi} = 0, \tag{5.46}$$

$$\alpha'\big|_0^{2\pi} = 0, \tag{5.47}$$

$$\alpha''\big|_0^{2\pi} = 0, \tag{5.48}$$

$$\alpha(\pi) = 0, \tag{5.49}$$

$$\alpha'(\pi) = 0. \tag{5.50}$$

Substitute (5.45) into (5.43), (5.48) and (5.47) into (5.44) and (5.45), respectively:

$$\alpha''' + \alpha^{(5)}\big|_0^{2\pi} = 0, \tag{5.51}$$

$$\alpha^{(4)}\big|_0^{2\pi} = -\frac{f}{2\tilde{E}}, \tag{5.52}$$

$$\alpha'''\big|_0^{2\pi} = 0. \tag{5.53}$$

Then we substitute (5.53) into (5.51):

$$\alpha^{(5)}\big|_0^{2\pi} = 0.$$

Finally, rewrite all conditions:

$$\alpha\big|_0^{2\pi} = 0, \tag{5.54}$$

$$\alpha'|_0^{2\pi} = 0, \tag{5.55}$$

$$\alpha''|_0^{2\pi} = 0, \tag{5.56}$$

$$\alpha'''|_0^{2\pi} = 0, \tag{5.57}$$

$$\alpha^{(4)}|_0^{2\pi} = -\frac{f}{2\tilde{E}}, \tag{5.58}$$

$$\alpha^{(5)}|_0^{2\pi} = 0, \tag{5.59}$$

$$\alpha(\pi) = 0, \tag{5.60}$$

$$\alpha'(\pi) = 0. \tag{5.61}$$

5.3.4.1 Simulation

This boundary problem is best solved using the finite difference method. We split the interval $[0, 2\pi]$ into N equal parts, each of width $\Delta = \frac{2\pi}{N}$. Since the differential equation (5.42) is linear, using the scheme of central difference, it reduces to

$$\alpha_{n+3} + (2\Delta^2 - 6)\alpha_{n+2} + (\Delta^4 - 8\Delta^2 + 15)\alpha_{n+1} + (-2\Delta^4 + 12\Delta^2 - 20)\alpha_n$$

$$+(\Delta^4 - 8\Delta^2 + 15)\alpha_{n-1} + (2\Delta^2 - 6)\alpha_{n-2} + \alpha_{n-3} = 0, \qquad \text{for} \quad n = 0, 1, \cdots, N.$$

To solve this problem numerically, we need to introduce unknowns α_{-3}, α_{-2}, α_{-1}, α_{N+1}, α_{N+2}, and α_{N+3}. We can eliminate these unknowns outside the interval where the original problem is posed by exerting the boundary conditions (5.54)–(5.59). Finally, we will create a system of linear equations which can be easily solved.

This bending only problem can also be solved using FEM. Denote by U_q the potential of the external load. We have

$$\begin{aligned} \text{min} \qquad &\frac{1}{2}ew \int_0^L (h\epsilon^2 + \frac{h^3}{12}\zeta^2)ds - U_q, \\ \text{subject to} \qquad &\frac{1}{2}ew \int_0^L h\epsilon^2 ds = 0. \end{aligned}$$

Imposing the bending only constraint requires the use of Lagrange multipliers. The problem
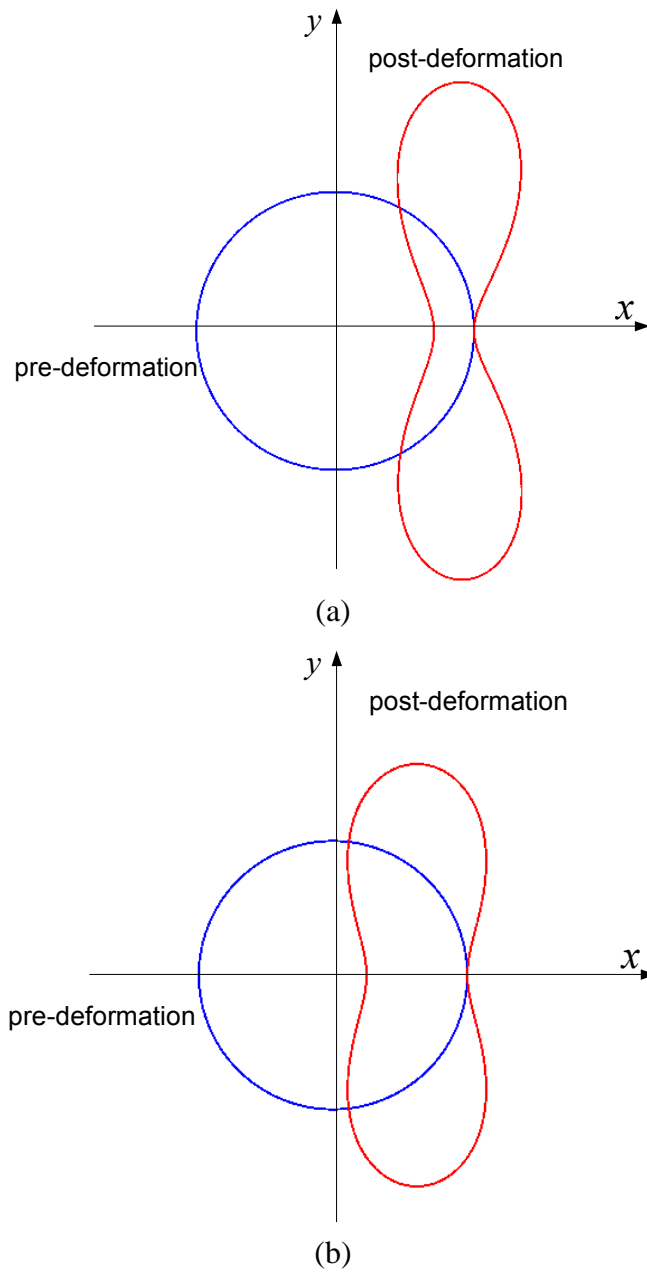
Figure 5.15 Deformation of a circle, (a) calculus of variations solution and (b)
FEM solution. It is anchored at rightmost point and squeezed at
leftmost point in the direction of the positive x-axis.

reduces to

$$\min \qquad \frac{1}{2}ew \int_0^L (h\epsilon^2 + \frac{h^3}{12}\zeta^2)ds - U_q + \lambda(\frac{1}{2}ew \int_0^L h\epsilon^2 ds).$$

Figure 5.15(a) shows the deformation of this circle obtained using calculus of variations. Figure 5.15(b) shows the results using FEM. The mechanical properties are the same for both methods. There is more cave-in for the calculus of variations solution. For an arbitrary shape curve, calculus of variations will be very difficult to implement because of the complexity of the high order differential equation. In comparison, FEM is applicable to any shape without increasing the complexity. Usually, energy minimization using FEM is numerically more stable. Meanwhile, exerting boundary conditions is more straightforward in the FEM solution compared with the calculus of variations one. Thus, FEM is preferred.

CHAPTER 6. CONCLUSION AND FUTURE WORK

In this chapter, we summarize our work, review contributions, and discuss the needed future work.

6.1   Conclusion

The first part of this thesis investigates deformable modeling of general shell-like objects. First, we describe the linear and nonlinear shell theories independently of a shell's middle surface parametrization, making them applicable to arbitrary parametric shells (and thus to freeform shells which are well approximated by spline or subdivision surfaces).[1] Second, we empirically compare our method with existing commercial software packages, establishing a convergence rate an order of magnitude higher. Third, we experimentally compare the linear and nonlinear elasticity theories in the context of a deformable object interacting with a robot hand, confirming that the nonlinear theory is more appropriate given large deformations often generated by the action of grasping.

Our modeling method is based on the physical theory of elasticity and experimental validated. It could potentially influence interactive computer graphics on achieving higher realism, especially on accurate computation of strain energy and deformation under applied force.

The second part of this thesis investigates two-finger squeeze grasp analysis of deformable curve-like objects. Both linear and nonlinear thin shell theories are reduced to be applicable

---

[1]The parametric independent formulation of strains also makes it possible to treat shells described by implicit equations, even though they are not common in practice.

to thin curved objects, which are essentially degenerate shells. This deformation modeling technique serves as the base for our analysis.

Under a squeeze grasp, the rotations of the finger contact friction cones depend on the global geometry of the object rather than on the local contact geometry. It is very difficult, if not impossible, to find a closed-form function that describes such a rotation in terms the force magnitude. Grasp analysis is best carried out by numerical procedures via energy minimization.

At some initially "not-graspable" positions, the squeeze force magnitude has to be above certain threshold in order to grasp a deformable object. Deformation plays a positive role in grasping of a deformable object. The set of "graspable" positions may increase compared to a rigid object which has the same geometry with the pre-grasp state of the deformable one.

The ability to resist disturbance is quite different between a grasp of a deformable object and that of a rigid one. With the magnitude of a disturbance force increasing, the grasp may be broken for the deformable object. In comparison, any disturbance force can be resisted by a force-closure grasp of the rigid object.

6.2   Future Work

Up to now, not many research efforts have been devoted to grasping of deformable objects. This thesis provides our initial work in this area. Along this promising line of research, there are several interesting and important future directions:

- *Grasp synthesis*. How to find the best graspable position under energy principles?

- *Grasp evaluation*. How to evaluate a deformable grasp? There are numerous metrics for graspings of rigid objects. However, most of them are not applicable to deformable grasp.

- *Area contact*. The frictional force and moment depend on the pressure distribution inside the contact area.

- *Solids*. Solid objects are more common to be grasped in our daily life.

BIBLIOGRAPHY

[1] J. H. Argyris and D. W. Scharpf, "The SHEBA family of shell elements for the matrix displacement method. Part I. Natural definition of geometry and strains," *Aeronaut. J. Roy. Aeronaut. Soc.*, vol. 72, pp. 873–878, 1968.

[2] D. Baraff and A. Witkin, " Large steps in cloth simulation," in *Proc. Comput. Graphics Interactive Tech., SIGGRAPH.*, 1998, pp. 43–54.

[3] A. Barr, Global and local deformations of solid primitives. In *Proceedings of ACM SIGGRAPH*, pages 21–30, 1984.

[4] R. Bartels, J. Beatty, and B. Barsky, *An Introduction to Splines for Use in Computer Graphics and Geometric Modeling*, Morgan Kaufmann, Los Altos, 1987.

[5] K. J. Bathe, *Finite Element Procedures*, Prentice Hall, 1996.

[6] T. Belytschko and C. Tsay, "A stabilization procedure for the quadrilateral plate element with one-point quadrature," *Int. J. Numer. Methods in Engrg.*, 19, pp. 405–419, 1983.

[7] A. Bicchi and V. Kumar, "Robotic grasping and contact: a review," in *Proc. IEEE Intl. Conf. Robot. Autom.*, 2000, pp. 348–353.

[8] A. Blake, "A symmetry theory of planar grasp," *Int. J. Robot. Res.*, vol. 14, pp. 425–444, 2004.

[9] G. M. Bone and Y. Du, "Multi-metric comparison of optimal 2D grasp planning algorithms," in *Proc. IEEE Int. Conf. Robot. Autom.*, 2001, pp. 3061–3066.

[10] M. Bro-Nielsen and S. Cotin, "Real-time volumetric deformable models for surgery simulation using finite elements and condensatoin," in *Proc. Eurographics*, 1996, pp. 57–66.

[11] J. Chadwick, D. Haumann, and R. Parent, "Layered construction for deformable animated characters," in *Proc. Comput. Graphics Interactive Tech., SIGGRAPH.*, 1989, pp. 243–252.

[12] F. Cirak, M. Ortiz, and P. Schröder, "Subdivision surfaces: a new paradigm for thin-shell finite-element analysis," *Int. J. Numer. Methods in Engrg.*, vol. 47, pp. 2039–2072, 2000.

[13] J. Collier, B. Collier, G. O'Toole, and S. Sargand, "Drape prediction by means of finite-element analysis," *J. Textile Institute*, vol. 82, pp. 96–107, 1991.

[14] J. J. Connor and C. A. Brebbia, "A stiffness matrix for a shallow rectangular shell element," *J. Eng. Mech. Div.*, vol. 93, pp. 43–65, 1967.

[15] F. Conti, O. Khatib, and C. Baur, "Interactive rendering of deformable objects based on a filling sphere modeling approach," in *Proc. IEEE Int. Conf. Robot. Autom.*, 2003, pp. 3716–3721.

[16] J. Cornellá and R. Suárez, "Fast and flexible determination of force-closure independent regions to grasp polygonal objects," in *Proc. IEEE Int. Conf. Robot. Autom.*, 2005, pp. 778–783.

[17] A. Dorfmann and R. B. Nelson, "Three-dimensional finite element for analyzing thin plate/shell structures," *Int. J. Numer. Methods in Engrg.*, vol. 38, pp. 3453–3482, 1995.

[18] Z. Doulgeri and J. Peltekis, "Modeling and dual arm manipulation of a flexible object," in *Proc. IEEE Int. Conf. Robot. Autom.*, 2004, pp. 1700–1705.

[19] G. Farin, *Curves and Surfaces for Computer Aided Geometric Design*. Academic Press, Inc., 2 edition, 1990.

[20] R. T. Fenner, *Engineering Elasticity: Application of Numerical and Analytical Techniques*. Ellis Horwood, Ltd., 1986.

[21] R. H. Gallagher, *Finite Element Analysis*. Prentice-Hall, Inc., 1975.

[22] P. G. Ciarlet, *The Finite Element Method for Elliptic Problems*. North-Holland, Amsterdam, 1978.

[23] S. F. Gibson and B. Mirtich, "A survey of deformable models in computer graphics," Technical Report TR-97-10, Mitsubishi Electric Research Laboratories, 1997.

[24] K. Gopalakrishnan and K. Goldberg, "D-space and deform closure grasps of deformable parts," *Int. J. Robot. Res.*, vol. 24, pp. 899–910, 2005.

[25] P. L. Gould, *Analysis of Plates and Shells*. Prentice-Hall, 1999.

[26] J. P. Gourret, N. Magnenat-Thalmann, and D. Thalmann, "Simulation of object and human skin deformations in a grasping task," in *Proc. Comput. Graphics Interactive Tech., SIGGRAPH.*, 1989, pp. 21–30.

[27] P. E. Grafton and D. R. Strome, "Analysis of axisymmetric shells by the direct stiffness method," *J. AIAA*, vol. 3, pp. 2138–2145, 1963.

[28] A. E. Green and W. Zerna, *Theoretical Elasticity*. Oxford at the Clarendon Press, 1968.

[29] A. M. Howard and G. A. Bekey, "Recursive learning for deformable object manipulation," in *Proc. International Conference on Advanced Robotics*, 1997, pp. 939-944.

[30] C. Holleman, L. E. Kavraki, and J. Warren, "Planning paths for a flexible surface patch," in *Proc. IEEE Int. Conf. Robot. Autom.*, 1998, pp. 21–26.

[31] S. Hirai, T. Tsuboi, and T. Wada, "Robust grasping manipulation of deformable objects," in *Proc. IEEE Symp. Assembly and Task Planning*, 2001, pp. 411-416.

[32] T. J. R. Hughes and W. K. Liu, "Nonlinear finite element analysis of shells: Part I. Three-dimensional shells," *Comput. Methods Appl. Mech. Engrg.*, vol. 26, pp. 331–362, 1981.

[33] D. L. James and D. K. Pai. Artdefo: accurate real time deformable objects. In *Proceedings of ACM SIGGRAPH*, pages 65–72, 1999.

[34] Y.-B. Jia, "Curvature-based computation of antipodal grasps," in *Proc. IEEE Int. Conf. Robot. Autom.*, 2002, pp. 1571–1577.

[35] Y.-B. Jia, "On computing optimal planar grasps," in *Proc. IEEE/RSJ Intl. Conf. Intell. Robots and Systems*, 1995, pp. 427–434.

[36] Y.-B. Jia and J. Tian, "Deformations of general parametric shells: computation and experiment," in *Proc. IEEE/RSJ Intl. Conf. Intell. Robots and Systems*, 2008, pp. 1796–1803.

[37] J. Kerr and B. Roth, "Analysis of multifingered hands," *Int. J. Robot. Res.*, vol. 4, pp. 3–17, 1986.

[38] A. Kamoulakos, "Understanding and improving the reduced integration of Mindlin shell elements," *Int. J. Numer. Methods in Engrg.*, vol. 26, pp. 2009–2029, 1988.

[39] A. Laulusa, O. A. Bauchau, J-Y. Choi, V. B. C. Tan and L. Li, "Evaluation of some shear deformable shell elements," *Int. J. Solids and Structures.*, vol. 43, pp. 5033–5054, 2006.

[40] A. M. Ladd and L. E. Kavraki, "Using motion planning for knot untangling," *Int. J. Robot. Res.*, vol. 23, pp. 797–808, 2004.

[41] Z. Li, S. S. Sastry, "Task-oriented optimal grasping by multifingered robot hands," *IEEE Trans. Robot. Automat.*, vol. 4, pp. 32–44, 1988.

[42] Y. H. Liu, M. L. Lam, and D. Ding "A complete and efficient algorithm for searching 3-D from-closure grasps in the descrete domain," *IEEE Trans. Robot.*, vol. 20, pp. 805–816, 2004.

[43] C. Loop, "Smooth subdivision surfaces based on triangles," M.S. thesis, Univ. Utah, 1987.

[44] A. E. H. Love, *A Treatise on the Mathematical Theory of Elasticity*. Dover, New York, N.Y., 4 edition, 1927.

[45] Q. Luo and J. Xiao, "Contact and deformation modeling for interactive environments," *IEEE Trans. Robot.*, vol. 23, pp. 416–430, 2007.

[46] M. T. Mason, *Mechanics of Robotic Manipulation*. MIT Press, 2001.

[47] T. Matsuno and T. Fukuda, "Manipulation of flexible rope using topological model based on sensor information," in *Proc. IEEE/RSJ Int. Conf. Intell. Robots and Systems*, 2006, pp. 2638–2643.

[48] T. McInerney and D. Terzopoulos, "Deformable models in medical image analysis: a survey," *Medical Image Analysis*, vol. 1, pp. 91–108, 1996.

[49] B. Mirtich and J. Canny, "Easily computable optimum grasps in 2-D and 3-D," in *Proc. IEEE Int. Conf. Robot. Autom.*, 1994, pp. 739–747.

[50] B. Mishra and M. Teichmann, "Three finger optimal planar grasps," in *Proc. IEEE/RSJ Int. Conf. Intell. Robots and Systems*, 1994.

[51] M. Moll and L. E. Kavraki, "Path planning for deformable linear objects," *IEEE Trans. Robot. Automat.*, vol. 22, pp. 625–636, 2006.

[52] M. Müller and M. Gross, "Interactive virtual materials," in *Proc. Graphics Interface*, 2004, pp. 239–246.

[53] A. Nealen, M. Müller, R. Keiser, E. Boxerman, and M. Carlson, "Physically based deformable models in computer graphics," *Computer Graphics Forum*, 2006, pp. 809–836.

[54] V. D. Nguyen, "Constructing force-closure grasps," *Int. J. Robot. Res.*, vol. 7, pp. 3–16, 1988.

[55] V. V. Novozhilov, *Foundnations of the Nonlinear Theory of Elasticity*. Graylock Press, 1953; Dover, 1999.

[56] V. V. Novozhilov, *The Theory of Thin Shells*. P. Noordhoff Ltd., 1959.

[57] B. O'Neill, *Elementary Differential Geometry*. Academic Press, Inc., 1966.

[58] D. K. Pai, "STRANDS: Interactive simulation of thin solids using Cosserat models," *Computer Graphics Forum*, 2002, pp. 347–352.

[59] A. N. Palazotto and S. T. Dennis, *Nonlinear analysis of shell structures*. American Institute of Aeronautics and Ast, 1992.

[60] G. Picinbono, H. Delingette, and N. Ayache, "Non-Linear and Anisotropic Elastic Soft Tissue Models for Medical Simulation," in *Proc. IEEE Int. Conf. Robot. Autom.*, 2001, pp. 1371–1376.

[61] N. S. Pollard, "Closure and quality equivalence for efficient synthesis of grasps from examples," *Int. J. Robot. Res.*, vol. 23, pp. 595–613, 2004.

[62] E. P. Popov, J. Penzien, and Z. A. Lu, "Finite element solution for axisymmetric shells," *J. Eng. Mech. Div.*, vol. 90, pp. 119–145, 1965.

[63] J. Ponce and B. Faverjon, "On computing three finger force-closure grasp of polygonal objects," *IEEE Trans. Robot. Automat.*, vol. 11, pp. 868–881, 1995.

[64] J. Ponce, S. Sullivan, A. Sudsang, J. D.Boissonnat, and J. P. Merlet, "On computing four-finger equilibrium and force-closure grasps of polyhedral objects," *Int. J. Robot. Res.*, vol. 16, pp. 11–35, 1997.

[65] J. Ponce, D. Stam, and B. Faverjon, "On computing two-finger force-closure grasps of curved 2D objects," *Int. J. Robot. Res.*, vol. 12, pp. 263–273, 1993.

[66] A. Pressley, *Elementary Differential Geometry*. Springer-Verlag, 2001.

[67] J. N. Reddy, *An Introduction to Nonlinear Finite Element Analysis*. Oxford University Press, 2004.

[68] J. N. Reddy, *An Introduction to The Finite Element Method*. Tata Mcgraw-Hill, 2006.

[69] A. Remde, D. Henrich, and H. Worn, "Picking-up deformable linear objects with industrial robots," in *Proc. Int. Symp. Robot.*, 1999.

[70] A. S. Saada, *Elasticity: Theory and Applications*. Krieger Publishing Company, 1993.

[71] M. Saha and P. Isto, "Motion planning for robotic manipulation of deformable linear objects," in *Proc. IEEE Int. Conf. Robot. Autom.*, 2006, pp. 2478–2484.

[72] L. Segerlind, *Applied Finite Element Analysis*. John Wiley and Sons, New York, 1984.

[73] J. Stam, "Evaluation of loop subdivision surfaces," in *Proc. Comput. Graphics Interactive Tech., SIGGRAPH.*, CDROM Proceedings, 1998.

[74] A. F. Stappen, C. Wentink, and M. H.Overmars, "Computing immobilizing grasps of polygonal parts," *Int. J. Robot. Res.*, vol. 19, pp. 467–479, 2000.

[75] D. Terzopoulos, J. C. Platt, and A. H. Barr, "Elastically deformable models," in *Proc. Comput. Graphics Interactive Tech., SIGGRAPH.*, 1987, pp. 205–214.

[76] D. Terzopoulos and K. Waters, "Physically-based facial modeling, analysis, and animation," *J. Vis. Comput. Animation*, vol. 1, pp. 73–80, 1990.

[77] B. Thomaszewski, M. Wacker, and W. Straßer, "A consistent bending model for cloth simulation with corotational subdivision finite elements," in *Eurographics/SIGGRAPH Symp. Comp. Animation*, pp. 107–116, 2006.

[78] J. C. Trinkle, "On the stability and instantaneous velocity of grasped frictionless objects," *IEEE Trans. Robot. Automat.*, vol. 8, pp. 560–572, 1992.

[79] J. Tian and Y.-B. Jia, "Modeling deformable shell-like objects grasped by a robot hand," in *Proc. IEEE Int. Conf. Robot. Autom.*, 2009, pp. 1297–1302.

[80] S. P. Timoshenko and S. Woinowsky-Krieger, *Theory of Plates and Shells*. McGraw-Hill, 2 edition, 1959.

[81] X. Tu and D. Terzopoulos, "Artificial fishes: physics, locomotion, perception, behavior," in *Proc. Comput. Graphics Interactive Tech., SIGGRAPH.*, 1994, pp 43–50.

[82] H. Wakamatsu, S. Hirai and K. Iwata, "Static analysis of deformable object grasping based on bounded force closure," in *Proc. IEEE/RSJ Intl. Conf. Intell. Robots and Systems*, 1996, pp. 3324-3329.

[83] H. Wakamatsu, E. Arai, and S. Hirai, "Knotting/unknotting manipulation of deformable linear objects," *Int. J. Robot. Res.*, vol. 25, pp. 371–395, 2006.

[84] H. Wakamatsu and S. Hirai, "Static modeling of linear object deformation based on differential geometry," *Int. J. Robot. Res.*, vol. 23, pp. 293–311, 2004.

[85] H. Wakamatsu, E. Morinaga, E. Arai, and S. Hirai, "Deformation modeling of belt object with angles," in *Proc. IEEE Int. Conf. Robot. Autom.*, 2009, pp. 606–611.

[86] K. Washizu, *Variational Methods in Elasticity and Plasticity*, Pergamon Press, 1968.

[87] K. Waters, "A muscle model for animating three-dimensional facial expression," in *Proc. Comput. Graphics Interactive Tech., SIGGRAPH.*, 1987, pp. 17–24.

[88] H. T. Y. Yang, S. Saigal, and D. G. Liaw, "Advances of thin shell finite elements and some applications — version 1," *Comput. Structures*, vol. 35, pp. 481–504, 1990.

[89] H. T. Y. Yang, S. Saigal, A. Masud, and R. K. Kapania, "A survey of recent shell finite elements," *Int. J. Numer. Methods in Engrg.*, vol. 47, pp. 101–127, 2000.

[90] Y. Zhuang and J. Canny, "Haptic interaction of global deformations," in *Proc. IEEE Int. Conf. Robot. Autom.*, 2000, pp. 2428–2433.

[91] O. C. Zienkiewicz, *The Finite Element Method*. McGraw-Hill, 3rd edition, 1979.